FLOW CONTROL IN AN ANNULAR-RETURN FLOW USING COMBUSTION-DRIVEN ACTUATORS

A Thesis
Presented to
The Academic Faculty

By

Dmitry Iosifovich Shlyubsky

In Partial Fulfillment
Of the Requirements for the Degree
Master of Science in
Mechanical Engineering

Georgia Institute of Technology

May 2006

FLOW CONTROL IN AN ANNULAR-RETURN FLOW USING COMBUSTION-DRIVEN ACTUATORS

Approved By:

Dr. Ari Glezer
Woodruff School of Mechanical Engineering
Georgia Institute of Technology

Dr. Thomas M. Crittenden
Woodruff School of Mechanical Engineering
Georgia Institute of Technology

Dr. Paul G. Neitzel
Woodruff School of Mechanical Engineering
Georgia Institute of Technology

Date Approved: January 6, 2006

DEDICATION

To my loving parents for their patience and support and my deceased grandfather and uncle who would have loved to see this day

ACKNOWLEDGEMENTS

I would like to express my deepest appreciation to Dr. Thomas Crittenden for being a wonderful mentor and for working alongside me, helping and advising me, during the design and data acquisition phases of this project. Furthermore, I would like to thank my thesis advisor Dr. Ari Glezer for his dedication in directing this project and editing this work. His guidance has been instrumental to the success of this project.

I am also grateful to NASA and the DOD for providing the financial support for this project as part of their URETI on Aero-Propulsion and Power Technologies. I would also like to thank Dr. Ben Zin and Dr. Yedidia Neumeier of the Georgia Tech Combustion Laboratory who obtained the funding for this project and whose vision inspired the work reported herein.

Finally, I would like to express my gratitude to my family for their continued love, support, and patients and to the wonderful friends (Jake Tompkins, Ben Hobson and Sharon Marshal) who permitted me to be their short-term roommate, during the composition of this work. Last, but not least, I would like to thank God for giving me the strength to complete this work, for now I have a deeper understanding of what Paul meant when he wrote " I can do all things through Christ who strengthens me".

TABLE OF CONTENTS

LIST OF TABLES

LIST OF FIGURES

NOMENCLATURE

x^*	Distance from the jet's exit plane measured in the streamwise (jet) direction
r	Radial distance from the centerline
r'	Radial coordinate of the contour of $U = 0$ as a function of x^*
U_o	Centerline velocity of jet at the jet's exit plane (Jet Speed)
U	Mean local axial velocity as a function of x^* and r
V	Mean local radial velocity as a function of x^* and r
u_H	Average speed of the countercurrent flow in the annular region surrounding the jet as a function of x^*
U_m	Centerline velocity as a function of x^*
R	Radius of annular tube
D	Diameter of annular tube
d	Diameter of the jet at the jet's exit plane ($x^* = 0$)

b	Thickness of mixing layer
b_o	Radius of the jet at the jet's exit plane
b^*	b/R
b_o^*	b_o/R which is equivalent to d/D
m	u_H/ U_o
L	Distance from the exit plane to the end-wall
M	Absolute value of the momentum flux in the streamwise (jet) direction across the vertical (radial) plane as a function of x^*
G	Mass flux across the vertical (radial) plane in any arbitrarily defined radial domain as a function of x^*
G_o	Mass flux in the streamwise (jet) direction of the primary jet at the exit plane
M_o	Momentum flux in the streamwise (jet) direction of the primary jet at the exit plane
u'	rms fluctuations of $u(r,x^*,t)$

v'	rms fluctuations of v(r,x^*,t)
P	Mean pressure at $x^* = L$ as a function of r
P'	rms fluctuations of the pressure p($x^* = L$, r, t)
P_r	Pressure ratio across actuator orifice
A	$(G - G_o)/G_o$
P_s	Stagnation pressure of primary jet at the exit plane

Greek Symbols

W	Azimuthal vorticity
F	Equivalence ratio
?	Fluid density
t_r	Chamber refill time
t_b	Burning time of the mixture

SUMMARY

The annular-return flow and the utility of small-scale, combustion–based actuators for its control are investigated experimentally. The annular return flow is generated by an axial primary round jet, which impinges normally on a bounded end wall of a concentric tube, subsequently reverses direction, and exits the tube in a countercurrent flow to the primary jet. The combustion–based actuator generates a momentary (pulsed) jet that is produced by the ignition of a mixture of gaseous fuel and oxidizer in a small (cubic centimeter scale) combustion chamber. The operating frequency and the phase can be continuously varied by independently controlling the flow rate of the fuel/oxidizer and the ignition frequency. Two radially-opposing actuators are mounted on the wall of the annular return tube and are used to trigger flow transients that alter the global flow through strong feedback.

The characteristics of the baseline flow and the effects of actuation are investigated using particle image velocimetry (PIV) as well as static and unsteady pressure measurements. The baseline flow is highly unstable, exhibiting very high rates of flow recirculation. The actuator jet acts as an azimuthal obstruction deflecting the primary jet and causing it to flow around the actuator jet. Furthermore, the interaction of the primary jet with the actuator jets generates large-scale circulation domains.

CHAPTER 1

INTRODUCTION

A special configuration of a normal impinging jet is an annular-return flow, in which a primary jet issues coaxially into a larger capped (dead-end) concentric tube. The primary jet induces a countercurrent flow that is formed by impingement and turning at the capped end of the annular tube (e.g. Abramovich, 1963). This flow is accompanied by the formation of an axisymmetric shear layer between the incoming jet and the annular exhaust flow. The purpose of the present investigation is to determine the characteristics of the flow field generated by injecting a turbulent jet into a circular dead-end tube and to evaluate the effectiveness of using combustion based actuators for modification of the baseline flow (e.g. recirculation and mixing). The velocity field in each configuration is measured using Particle Image Velocimetry (PIV) at several axial cross sections for the baseline and forced flow. The pressure distribution on the end-wall is measured using arrays of static pressure ports.

A combustion-based actuator produces a momentary (pulsed) jet by the ignition of a mixture of gaseous fuel and oxidizer in a small [O (1cc)] combustion chamber. The actuator generates a brief [O (1 ms)], high-impulse jet through a small orifice in the combustor. The operating frequency of the resulting jet can be continuously varied by controlling the flow rate of the fuel/oxidizer and the ignition timing.

The investigation of the countercurrent flow geometry is motivated by an effort at Georgia Tech to reduce emissions and increase the fuel efficiency in flameless combustors of this basic geometry. As stated by Bruno and Vallini (1999), Flameless

oxidation is a recently discovered combustion regime that has been shown to reduce NOx emissions while decreasing fuel consumption, when implemented in atmospheric furnaces. It is characterized by the mixing of the fuel/air mixture with hot exhaust gases at very high recirculation rates. To maintain a stable flame in a gas turbine, exhaust flow recirculation is used to anchor the flame. Typically, this is accomplished with recirculation rates of less than 30%. If the recirculation rate is much higher, flameless oxidation can be achieved under certain conditions. Hence, flameless oxidation may be regarded as the next step in the recirculation anchoring of flames, provided adequate flow recirculation can be achieved. Efforts to investigate the application of a dead-end annular-return flow, as a method of recirculation based flame anchoring are currently underway at Georgia Tech.

CHAPTER 2

TECHNICAL BACKGROUND

2.1 Theory

Annular countercurrent flow has been of substantial interest for controlled efficient mixing processes. Abramovich (1963) developed theoretical solutions for jets issuing into infinitely long rectangular and axisymmetric dead-end chambers. The discussion of his theory herein, referring only to the axisymmetric geometry with an axisymmetric jet (Figure 2.1). Abramovich divides the flow into three regions. Near the exit plane, the centerline velocity is invariant, while the thickness of the region where the jet mixes with the counter-flow increases at a fixed rate. In the second region, the mixing zones are merged into a turbulent jet that continues to spread at a fixed rate as the centerline velocity decays. Finally, the fluid in the jet turns before reaching the end-wall in the third region, resulting in a region of stagnant fluid between the stagnation point and the end-wall.

As the jet spreads, the mass flow in the streamwise (jet) direction increases due to entrainment. Since mass is conserved across any plane that is normal to the jet axis, the net mass flux at each section is zero, and the mass flow in the annular, counter-flowing stream is equal to the jet mass flow. The transition between the second and third flow regions occurs where the maximum flow rate in the jet direction is reached. According to

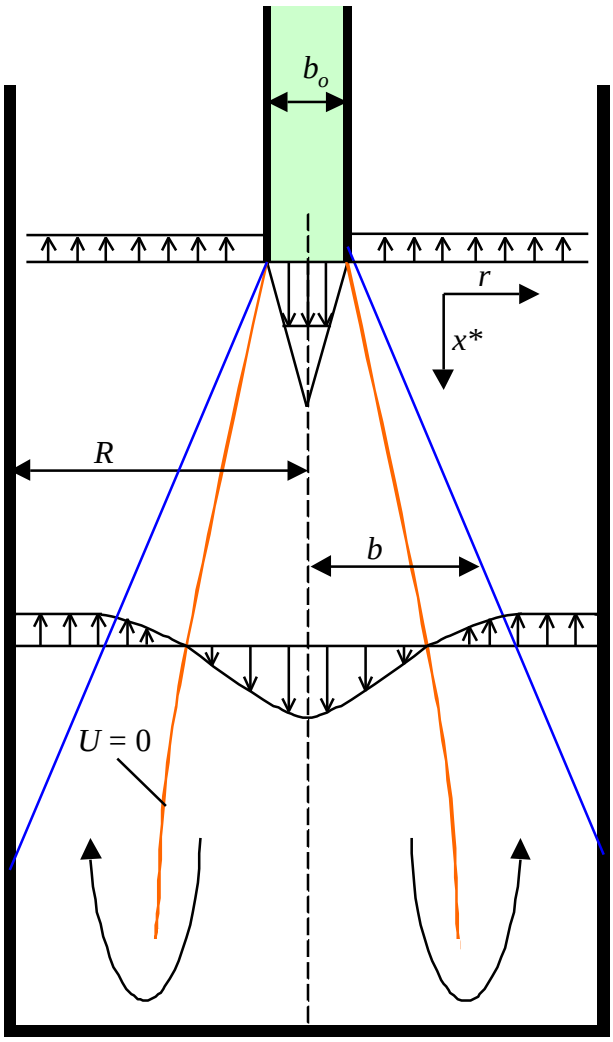

Figure 2.1 Conceptual sketch of axisymmetric, dead-end annular-return flow as described by Abramovich (1963)

calculations based on this analysis, this transition occurs 4.25*R* downstream of the injection plane. This point approximately corresponds to the position where $U = 0$ at $r/R = 0.707$.

The analytical solution associated with this theory utilizes the integral forms of the continuity and the momentum equations for an inviscid, isobaric flow. The equations for the centerline velocity (U_m) and the mixing zone thickness (b) at locations in which $x^*/R < 4.0$ in an axially symmetric configuration are shown below.

$$b^* = \sqrt{\frac{m}{0.258(1-m)}} \approx 0.26 \times \left(\frac{x^*}{R} \right) \qquad \text{(Abramovich 1963)} \qquad (1)$$

$$U_m / U_o = \sqrt{-0.258 \left(\frac{\left(b_\circ^*\right)^2}{1-\left(b_\circ^*\right)^2} \right) \frac{1-m}{m\left(0.14 - 0.02\,m - 0.118\,m^2\right)}} \quad \text{(Using negative m)} \qquad (2)$$

Abramovich (1963) reports that a comparison of the measured centerline velocity to the centerline velocity predicted by these equations shows considerable discrepancies between the experimental data and theoretical predictions at $x^*/R > 3.5$ ($x^*/R = 0$ at the injection plane).

2.2 Experimental and Numerical Investigations

White et al. (1975) report velocity measurements and flow visualization on a low-Reynolds-number (Re < 1300) jet exiting into a short (L/D =1.0) dead-end chamber using line traces of seeding particles. The flow visualization indicates that the flow may be

characterized by: (a) a jet on the axis; (b) a slow countercurrent flow in the annular region external to the jet; and (c) a toroidal vortex located in the corner between the annular wall and the end-plate. Vorticity levels in the toroidal vortex are determined from the velocity measurements. The resulting vorticity field was used to solve the vorticity equation and the equation proposed in Batchelor's asymptotic theory (Batchelor, 1956) for steady laminar flow. White et. al. conclude that the toroidal vortex is driven by the jet in equilibrium with its viscous drag in accordance with Batchelor's theory.

Another experimental investigation (Eckmann et al. 1996) focuses on a laminar (Re < 400) axisymmetric jet issuing into a long dead-end channel (L/D = 24). Eckmann et al. assert that PIV velocity measurements and flow visualizations demonstrate that the fluid near the center of the jet travels the furthest before reversing direction ahead of the end-wall, while the fluid at the outer edge reverses direction much closer to the jet tube outlet. Furthermore, the fluid in the jet turns before reaching the end-wall, resulting in a region of stagnant fluid between the stagnation point and the end-wall. The jet not reaching the end-wall is in agreement with the results obtained by Abramovich (1963) for an axisymmetric jet issuing into a infinitely long dead-end tube. Eckmann et al. report that when the jet is laminar penetration increases with the Reynolds number. However, high Reynolds number (turbulent i.e. Re > 2000) jets are not investigated in detail. Furthermore, Eckmann et al. state that for a fixed Reynolds number the penetration decreases slightly as the as d/D increases, and that some of the fluid is trapped in a long annular recirculation cell near the exit of the jet tube as the fluid exits the dead-end chamber.

The flow of a turbulent, axisymmetric jet into a dead-end tube was investigated numerically by Amano (1996). The velocity field, Reynolds-stresses, turbulent kinetic energy and the shear stresses on the surface of the annular tube are computed for $b_o^* = 0.189$ using a second-order-closure turbulence model (Amano,1986). The decay of the centerline velocity computed by this model matched the experimental data shown in Abramovich (1963) more closely than the analytical solution (Abramovich, 1963). Distributions of shear stress on the annular wall are only slightly affected by the Reynolds number and decrease as the distance between the injection plane and the end-wall (*L/D*) increases. However, the shear-stress distribution is significantly affected by the annular diameter. In fact, the location of the maximum shear stress migrates toward the end-plate and then flattens out as the annular diameter increases. Furthermore, the stagnation pressure on the end-plate decreases as the length of the channel increases until it reaches a minimum value (the terminal stagnation pressure), which increases as the annular diameter decreases. Finally, the turbulence is nearly isotropic throughout most of the flow, except near the inlet/outlet plane.

The experimental studies on the exit of jets into dead-end channels and the numerical study mentioned above indicate that this flow configuration exhibits two regimes. In the first, the jet does not penetrate far enough to impinge on the end-plate, while in the second the jet impinges on the end-plate. For given values of *L/D* and *d/D*, the flow will exhibit the characteristics of the second regime if *L/D* is smaller than the value associated with the penetration length. Based on the results reported by Eckmann et al. (1996), the *L/D* associated with the penetration length increases with Reynolds number for laminar jets. The analytical solution (Abramovich, 1963) indicates that the

penetration length is invariant with the Reynolds number when the jet is turbulent. In the present investigation, the jet impinges on the end-wall forming a confined wall jet.

2.3 Jet Impingement on Flat Plates

Landreth and Adrian (1990) used particle-image velocimetry (PIV) to obtain instantaneous velocity fields of the wall jet produced by the impingement of an axisymmetric jet (Re = 6,564) on a normal flat plate. Vector maps of the jet velocity field show that along the centerline the jet acts much like a stagnation point flow, forming a radial wall jet. A complex pattern of primary vortices, originating in the shear layer between the jet and the surrounding ambient air, approach the plate and are transported in the radial direction by the radial wall jet. As they translate along the plate, the origins of the vortices lie approximately 0.5*d* above the surface of the wall. Due to viscous effects at the wall, secondary vortices are produced generating a region where the sign of the vorticity is opposite that of the primary vortices. The boundary layer of the wall jet undergoes separation at a radial distance of 1.8*d* from the stagnation line. Consequently, the secondary vortices break away from the wall at a radial distance between 1.9*d* and 2.3*d*.

Ueda et al. (1997) used laser-doppler velocimetry (LVD) to study the impingement of a uniform, axisymmetric jet on to a flat plate. Instantaneous values of streamwise and radial velocity along the stagnation line are used to determine the mean and fluctuating velocities as well as the skewness, flatness, and histograms of the velocities. The rms value of fluctuating velocities in the streamwise direction decreases

monotonically with decreasing distance from the wall while the rms value of radial fluctuating velocity increases and reaches a maximum at the wall. The histogram of the fluctuating radial velocity near the wall is bi-modal. Ueda et al. demonstrate that the bi-modal distribution is the result of an organized motion of the stagnation streamline along the plate's surface following a circular path, which is concentric with the plate.

Although, the flow of an axisymmetric jet into a dead-end channel has been the subject of several experimental investigations, the characteristics of the velocity field have not been fully explained. In addition, there seems to be no previous record of the response of such a flow field to external forcing.

2.4 Combustion Driven Actuators

The combustion-driven jet actuator was first described and characterized by Crittenden, et al. (2001), and subsequently was used to demonstrated transient reattachment of separated flows by Funk, et al. (2002). The device (shown schematically in Figure 2.2 (Crittenden, et al. 2001)) yields a momentary high momentum jet by exploiting the chemical energy of the gaseous fuel/air mixture. A small (cm^3 scale) arbitrary-shape combustion chamber bounded by an orifice plate is filled by premixed fuel/oxidizer having relatively low momentum. A spark ignites the mixture, creating a high pressure burst within the combustor and a subsequent jet from one or more exhaust orifices. At the design scales, the entire combustion process is complete within several milliseconds and the cycle resumes with fresh fuel/oxidizer mixture entering the chamber and displacing the remaining combustion products. The cycle frequency is set by the

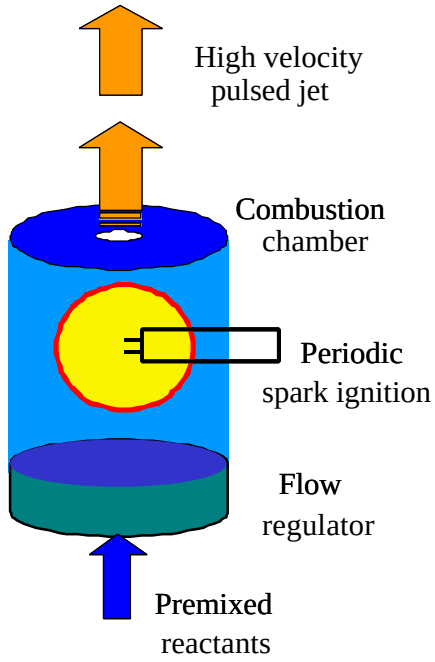

Figure 2.2 Conceptual illustration of combustion-driven jet actuator (Crittenden, et al. 2001).

spark/ignition source and is continuously variable up to a maximum frequency dictated by the combined burning time t_b of the mixture and chamber refill time t_r. The device has been operated with hydrogen, propane, acetylene, and natural gas as fuels, and, for a 1 cm^3 combustor, operating frequencies in excess of 150 Hz have been demonstrated using hydrogen/air mixtures. An important feature of this concept is that these combustors can be fabricated in high power, low weight, individually addressable arrays that can be operated over a broad frequency range. Because of the flexibility of the shape of the combustion chamber, actuator arrays can be conformed and integrated into surfaces of arbitrary shapes.

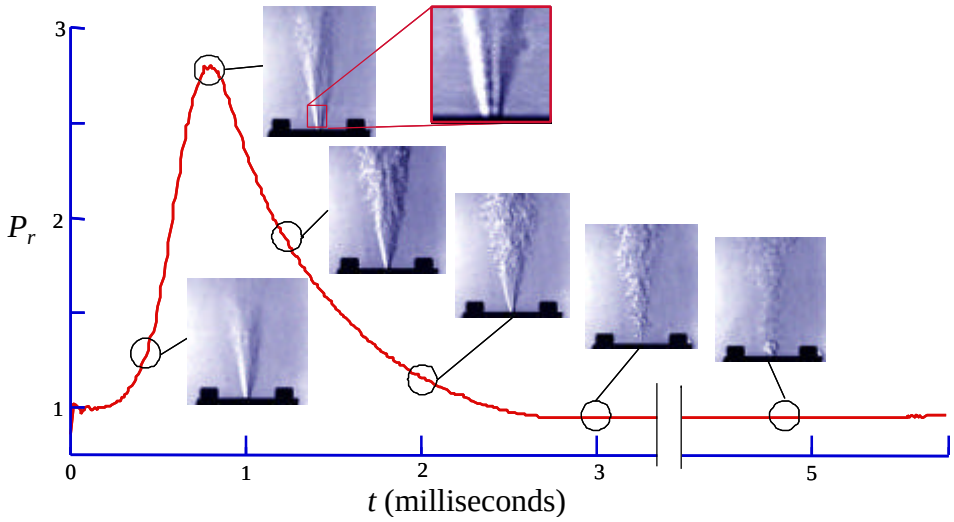

Figure 2.3 Phase-locked Schlieren images and pressure trace for 1 cm^3 combustion chamber with stoichiometric hydrogen mixture and 1.27 mm orifice diameter (Crittenden, et al. 2001).

The current configurations are based on passive fluidic valves for regulation and the actuator is operated with no moving parts of any kind. Typical performance characteristics for the combustion actuator are shown in Figure 2.3 (Crittenden, et al. 2001), featuring a sequence of phase-locked Schlieren images of the ejected jet during the combustion cycle relative to the pressure time-history. The pressure is plotted as the ratio between the chamber pressure and the ambient (for this case, equivalent to citing the pressure in atmospheres), and the images are taken at 0.44, 0.70, 1.2, 2, 3, and 4.8 ms following the spark trigger (using a 100 μs shutter speed) with a streamwise field of view of approximately 25 orifice diameters. Within the combustion cycle, the jet speed downstream of the exit plane varies from subsonic to supersonic and then becomes subsonic again before it decays as the combustor pressure returns to atmospheric (within approximately 3 ms). The jet flow in the far field is highly turbulent as is evidenced by the existence of small-scale structure. An enlarged view of the flow near the jet exit plane

at 0.7 ms (near the peak pressure) suggests the presence of cellular shock structures within approximately 5 orifice diameters (6 mm) downstream of the jet exit plane. Although this image is somewhat smeared due to the fluid motion and the variation in combustor pressure during the shutter opening time, their appearance coincides with the period in which the pressure level is sufficient to generate sonic speed at the orifice (i.e., pressure ratio > 1.89). Note that when the refill of the combustor begins (approximately 4 ms following the ignition spark) a weak starting vortex followed by a weak jet of combustion products (remnants from the cycle that is just completed) appear near the jet exit plane.

The specific pressure curve properties of the actuator (and the strength and duration of the resulting actuation jet) are affected by a number of different parameters including the fuel and mixture ratio (which affect the chemical energy available per unit volume and the chemical reaction rate), chamber volume (which governs the total amount of energy released and the duration of the reaction), exhaust orifice diameter (which determines the rate at which products exit the combustion chamber permitting the reactants to flow in), and chamber surface area (which affects the heat transfer losses to the walls and radical quenching effects). The peak pressures, phase-averaged at a low-frequency ignition rate, for a 1 cm^3 cylindrical chamber (with height-to-diameter ratio of 1.27) for variation in both mixture ratio and orifice diameter, using hydrogen-air mixtures, are shown in Figure 2.4 (Crittenden, et al. 2001). In general, it is noted that leaner mixture ratios produce lower peak pressure values, as do larger exhaust orifice sizes. The trend for variation in mixture ratio follows closely the pressure change

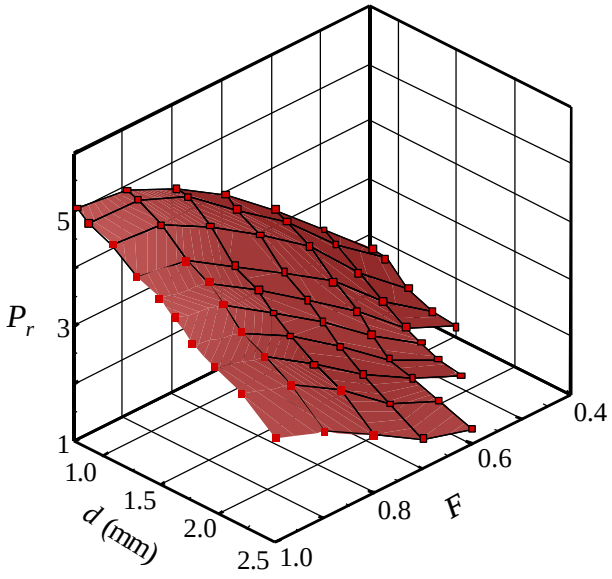

Figure 2.4 Surface plot of variation of the phase-averaged peak pressure with F and d for hydrogen in 1 cm^3 combustor (Crittenden, et al, 2001).

calculated for an idealized constant volume combustion process, but with a significant reduction that increases with increasing orifice diameter.

The phase-averaged pressures (Crittenden, et al. 2001), measured during the combustion process within the actuator, are shown in Figure 2.5 for varying mixture ratios (F), from stoichiometric to fuel-lean conditions. These data are measured using an Endevco piezoresistive, high-temperature pressure transducer, mounted into the wall of the combustor, with the spark trigger signal recorded to provide timing and phase data. For a stoichiometric mixture (F = 1.0), the peak pressure ratio is 3.26, well above the level required to produce sonic velocity at the orifice (P_r = 1.89), and the duration of the

pressure pulse is approximately 2.3 ms. As the mixture becomes leaner, lower peak values and longer pulse duration occur, down to F = 0.5 (the lowest level at which combustion was reliably observed) where the peak pressure ratio is 1.53 and the pulse duration is 4.2 ms. Varying the mixture ratio thus allows significant modification of the pressure pulse to achieve desired jet speeds. Other secondary factors affecting the combustion process include the frequency of the combustion bursts, the flow properties within the chamber (e.g., velocity and turbulence intensity), and the ignition location and energy. The effects of these parameters are discussed in detail in Crittenden (2003).

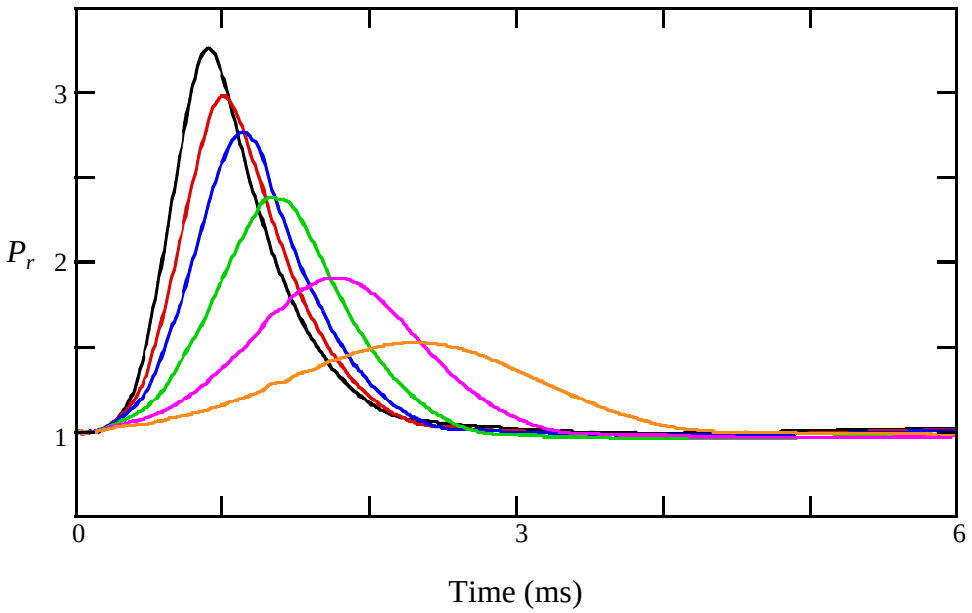

Figure 2.5 Phase-averaged pressure for present actuator geometry for hydrogen with F = 1.0 (—), 0.9(—), 0.8 (—), 0.7 (—), 0.6 (—), and 0.5 (—).

CHAPTER 3

EXPERIMENTAL FACILITIES AND PROCEDURES

3.1 Annular-Return Flow Facility

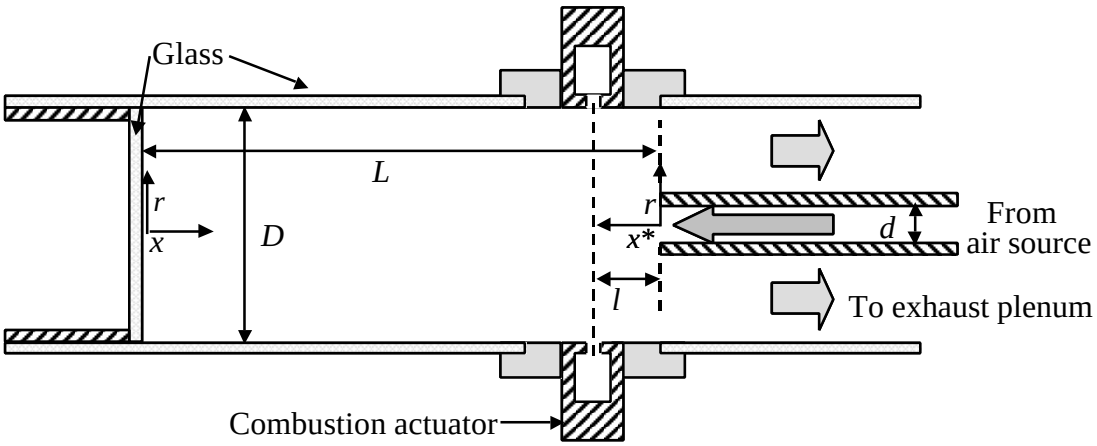

Figure 3.1. Schematic illustration of annular-return flow experiment.

The annular-return test facility is shown schematically in Figures 3.1 and 3.2 and in the photographs in Figures 3.3, 3.4, and 3.5. It is comprised of segments of glass and aluminum tubes (inner diameter D = 70 mm) that are joined by an acrylic coupler of the same inner diameter. These components are held together in the axial direction by an end-flange which is connected to the exhaust manifold by four 12.7 mm thick aluminum spacer-rods (Figures 3.2 and 3.3).

The primary jet is injected through a 76 cm long tube, having an inner diameter d = 8.9 mm (d/D = 0.127) and outer diameter of 9.5 mm, that is concentric to the annular-return tube and can be moved along its axis. The end of the jet tube is held level and

concentric by a stainless-steel collar that is supported by three stainless steel cables, arranged azimuthally at 120^o (Figure 3.4), and the tension in the cables is adjustable.

For the present experiments, two coordinate systems are used: x indicates the distance from the end-plug and x^* indicates the distance from the jet tube. As the air exits the test section, it enters a 32.7 cm (about 4.5D) long PVC pipe that forms the inner channel of the exhaust-plenum located 10 cm (about 1.5D) from the actuator orifices in the x direction (Figure 3.2). The air then flows into the external shell of the exhaust plenum through a 3.2 mm gap between the end of the inner channel and the rear flange and then exits the system through the exhaust-hose. Movable (telescopic) end-plugs are used for both PIV and pressure measurements, such that the distance L between the exit plane of the jet and end-wall can be continuously varied. The axial position of the jet tube is also adjustable, so that the distance between the end-wall and the jet tube as well as the distance between the jet tube and the actuator orifices (l) can be varied independently.

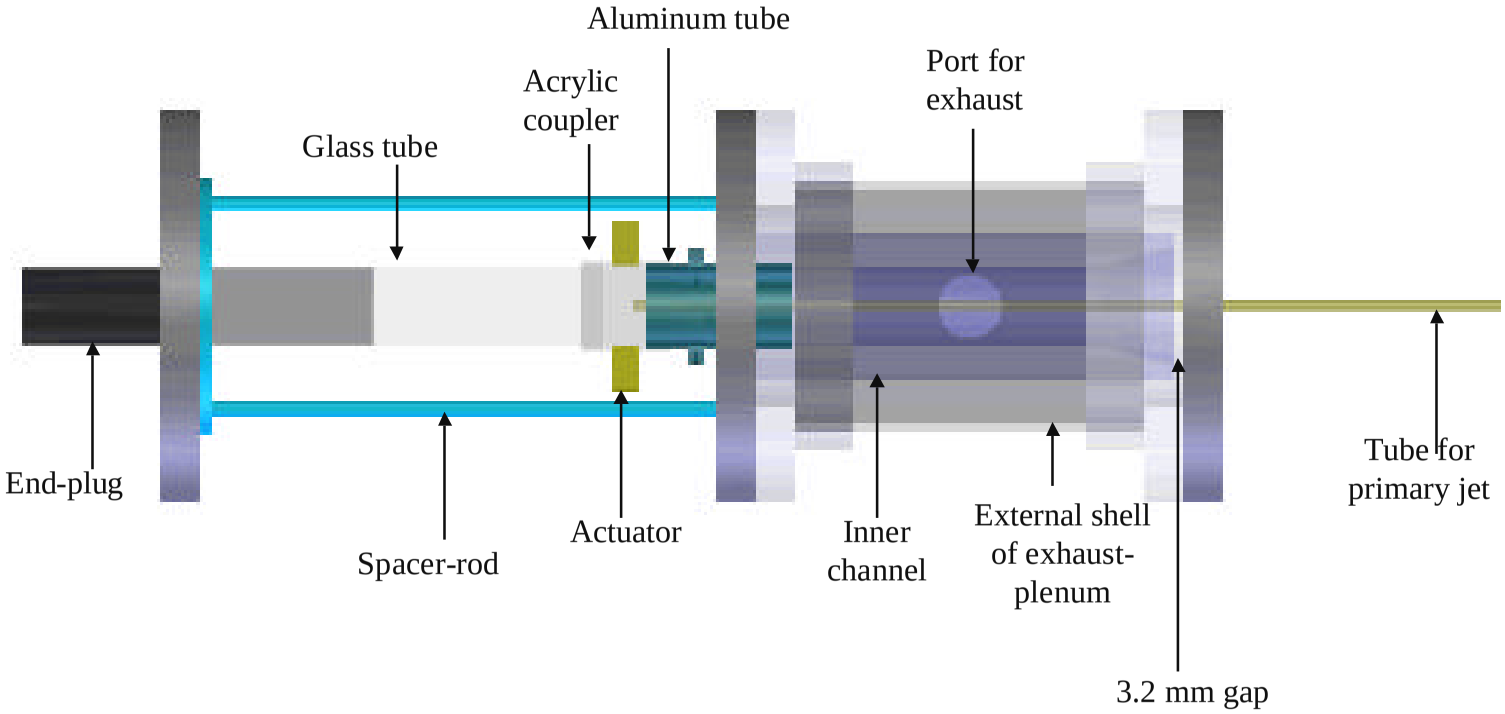

Figure 3.2 Schematic of the overall assembly for the annular-return flow facility.

Figure 3.3 Photograph of the annular-return flow facility.

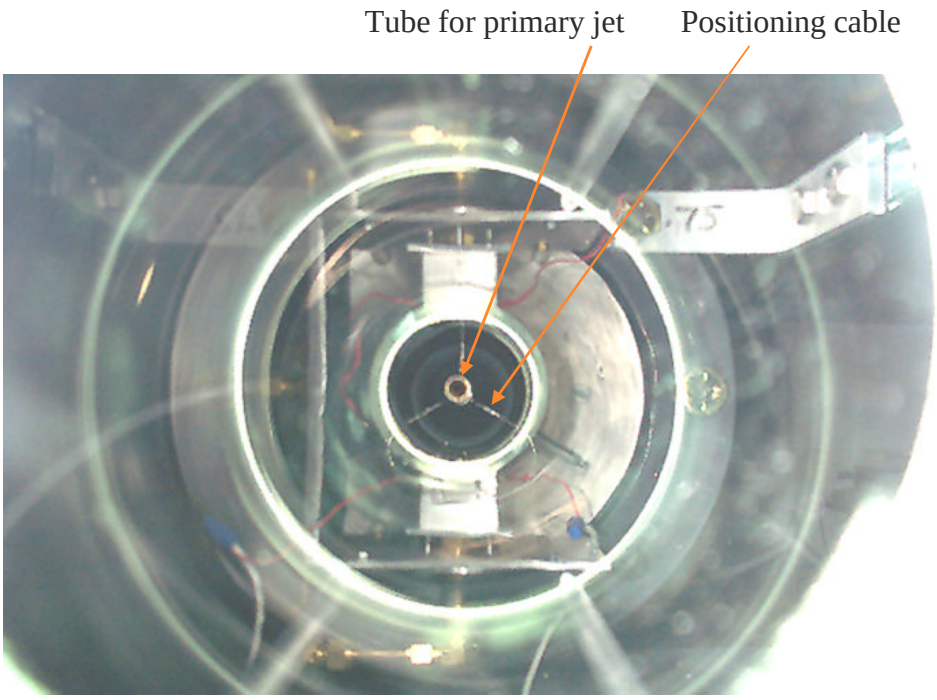

Figure 3.4 Positioning cables for the primary jet tube.

3.2 Actuator Assembly

The present experiments utilize two combustion-based actuators (Crittenden, et al. 2001). These actuators consist of a small (1 cm^3 scale) combustion chamber bounded by an orifice plate, which is filled by a fuel/oxidizer mixture. A spark ignites the mixture, creating a high-pressure burst within the combustion chamber and a subsequent jet from one or more exhaust orifices. The two combustion-driven actuators are inserted into slots, machined into the acrylic coupler, and the assembly is held together as a modular unit by the structural support bracket shown in Figures 3.5a and 3.5b. This structural support bracket fits into the space between the spacer-rods, and the acrylic coupler fits onto the aluminum tube segment tightly, resulting in a rigid well-centered assembly. The actuators are mounted such that their orifices are facing each other along the diametric line of the annular tube, that is in the plane defined by the axial (x^*) and radial (r) coordinates.

A schematic of the actuators used for the present experiments is shown in Figure 3.6. Each actuator is comprised of a cylindrical combustion chamber, having a volume of 1 cubic centimeter and a height-to-diameter aspect ratio of 1.5. The 1.2 mm diameter actuator orifice is concentric with the cylindrical walls. The spark-gap is 2 mm and is located at the geometric center of the chamber. The actuator frequency can be varied up to 150 Hz (Crittenden, 2003). For the purposes of this investigation, a stoichiometric mixture of hydrogen and air is used at a rate of 1 L/min in each actuator.

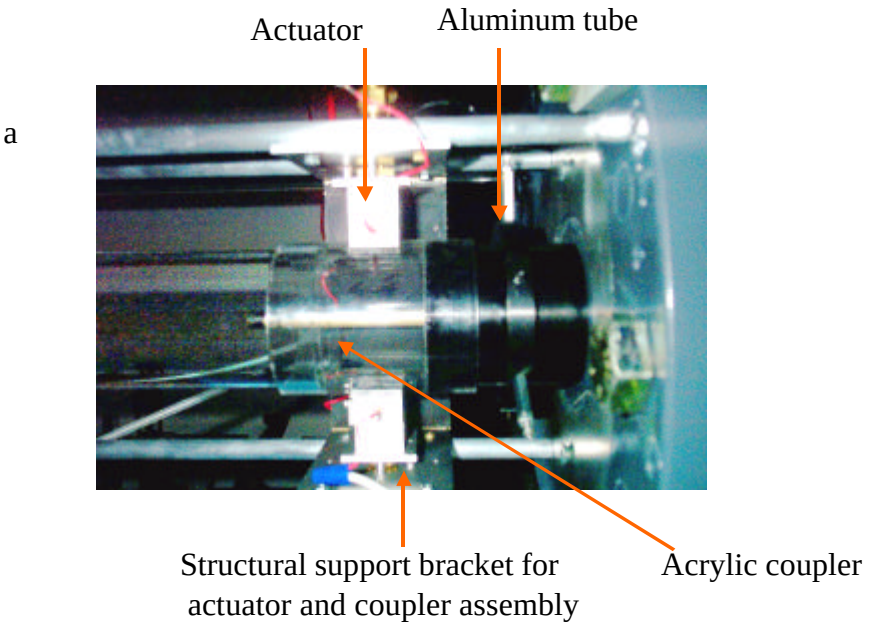

Figure 3.5 Actuator assembly (a) and interrogation region (b).

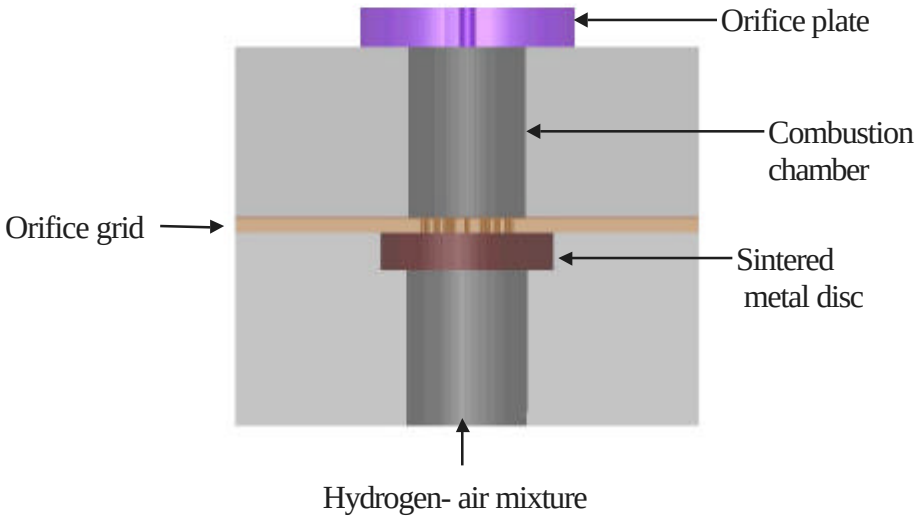

Figure 3.6 Cross-section of combustion driven actuator.

The fuel-air mixture is supplied to the actuators via the system illustrated in Figure 3.7. The pressures of the hydrogen and air streams are regulated independently to 40 psig. The flow rates are set by Aalborg (model #GFC171) thermal mass flow controllers, which are calibrated for air and hydrogen with flow capacities of 15 L/min and 2 L/min, respectively. The streams are then mixed and fed to the two actuators. The analog 0-5 VDC control signals for the flow controllers are generated by a dual output DC power supply (Hewlett Packard #E3620A). The mixture is ignited with a spark produced by a modified automotive ignition system, consisting of an ignition coil and a commercially available control circuit, triggered by a TTL signal, as described in Crittenden (2003). The TTL signal to the bottom actuator triggers the signal to the top actuator at user-specified time delays.

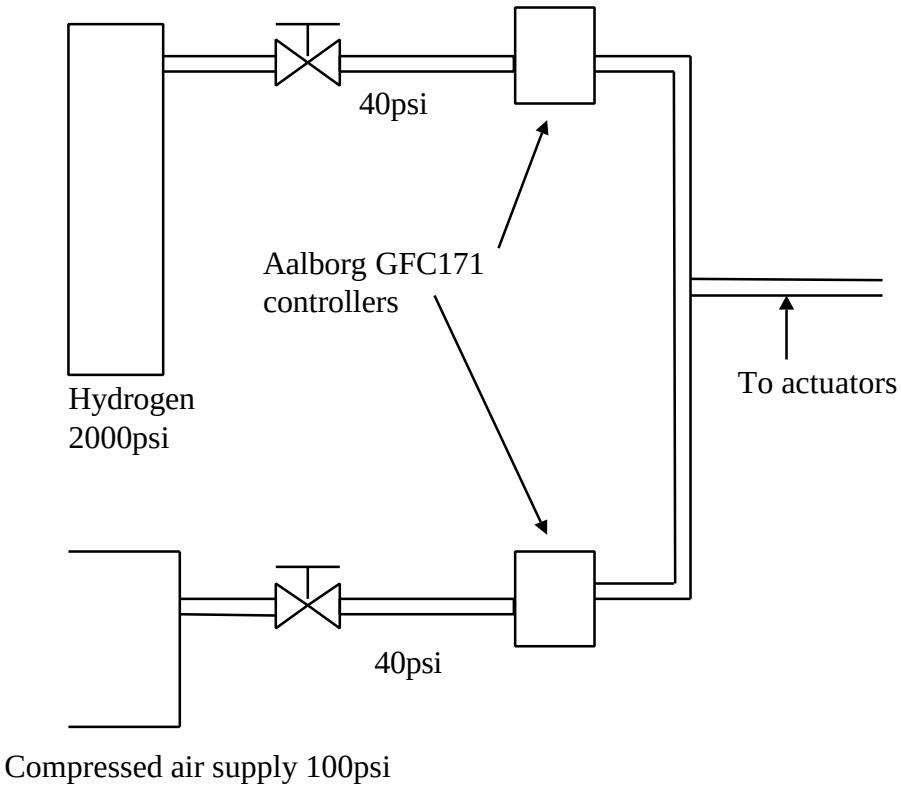

Figure 3.7 Process flow diagram for fuel-air mixing system.

3.3 Flow Supply/Seeding System

The primary jet is driven from a local compressed air source and is seeded with submicron fog particles (for particle image velocimetry), generated by a Rosco Model #1700 fogger. Due to the back-pressure in the primary jet tube (~2.0 psi), the fog is drawn in through a Vaccon (Model # JD-200M) Venturi vacuum pump installed in the air supply line. A portion of the supply air is diverted around the vacuum pump through a by-pass line, making it possible to adjust the seeding concentration independently of the jet speed.

The flow rate through the inlet of the venturi device is set using an Aalborg Model #GFC471 thermal mass flow controller with a flow capacity of 100 L/min. During PIV measurements, the flow rates through the by-pass line are set with an Aalborg Model #GFC671 controller with a flow capacity of 500 L/min. The set points of the controllers are calibrated by measuring the static suction on the intake with a vacuum gauge and the jet centerline velocity at the exit plane using a hot wire sensor. For all of the other test cases, the flow rates in the by-pass line are set with an Aalborg Model #GFC57 flow controller with a flow capacity of 200 L/min. The controllers enable setting the primary jet speed to within 1.5 m/s of the nominal jet speed.

3.4 PIV Measurements

The velocity field is studied using particle image velocimetry (PIV) (Raffel et al., 1998). The laser system used in these experiments is a 50mJ Nd:Yag (New Wave Research Minilaser 3-15), which has a maximum rate of 15 Hz. A laser sheet is formed by an optical set up and directed into the test section along its axis of symmetry by two mirrors mounted on a vertical support. The laser sheet is introduced along the centerline through glass windows that are installed into the telescopic plug at both ends. The flow is viewed normal to the cross-stream plane through the curved (cylindrical) surface of the annular tube. Due to the small rate of divergence of the laser sheet (1.2^{o}), the plug used for PIV measurements is made of thin walled stainless steel pipe. To maximize the length of the region in which the laser sheet touches the wall two diametrically opposed 95.25mm long x 6.35mm wide slits are cut into the wall along the axial direction. While in the present results the images are not corrected for cross-stream distortion, this may be done by capturing a grid target in the plane of the light sheet. Estimates using this technique show that the radial distortion in the image is negligible within the central section of the tube ($r/D = 0.43$).

The PIV images are captured using a 1000 x1016 pixel CCD camera (PIVCAM 10-30 Model #630046 by TSI). Two Nikon 60 mm and 105 mm lenses are used for full and zoomed views, respectively. The data are typically taken in several partially overlapping windows that are used to form full-field composites. The camera is mounted on a traverse that allows for adjustments of its vertical and streamwise position.

The sequence and timing of the trigger signals for the lasers, the camera and the time delay (dt) between the laser pulses is controlled by a TSI model #610032 synchronizer that is operated using Insight PIV software. In experiments that utilize the combustion actuators, the PIV data acquisition system is phase-locked to the actuator trigger signal. At each measurement station, PIV data are taken over 500 realizations, and the velocity vectors are calculated using a standard two-frame cross-correlation technique. Subsequently, the rms velocity fluctuations and the azimuthal vorticity (in cylindrical coordinates) are computed.

3.5 Pressure Measurements

The time-averaged pressure distribution on the surface of the end-wall is measured to determine the axial symmetry of the flow field. A scanning valve and a Baratron pressure sensor are used to measure the pressure over an array of 23 pressure ports on the end-wall, arranged on a 70 mm long diametric line (equally spaced with a center to center spacing of 3 mm), as shown in Figure 3.8a. 10 mmHg and 100 mmHg sensors are used for $L \geq 102$ mm and $L = 51$ mm, respectively, at a jet speed of 55 m/s. For a jet speed of 25 m/s, 1 mmHg and 10 mmHg sensors are used for $L \geq 102$ mm and $L = 51$ mm, respectively.

The response of the flow field to actuation is assessed using simultaneous time-resolved pressure measurements on the centerline (port #0) and at four equally spaced points 17.5 mm from the center (ports #1-4) (Figure 3.8b). Pressures are measured using

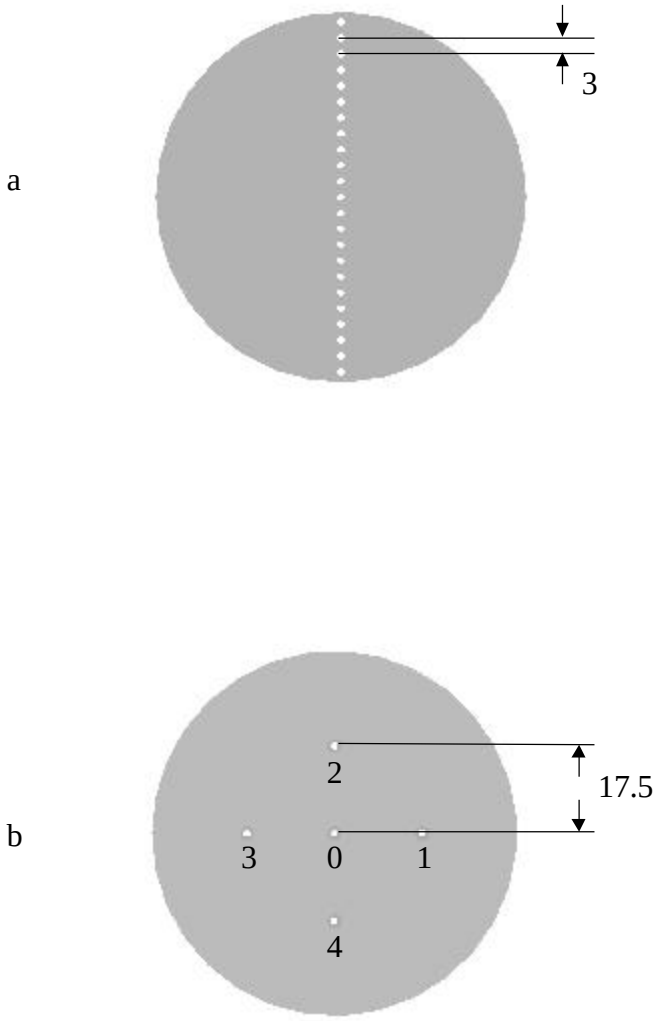

Figure 3.8 End-plates for measuring the mean pressure distribution (a) and the time dependent variation of the pressure for ports #0 - 4 (b).

SenSym SDXL010D DIP packaged pressure sensors (0-10 in of water), having a response time of 100 μSec. The output of the SenSym sensors is sampled at 5 kHz and the calibration curve for these sensors is shown in Figure 3.9. This calibration curve is a plot of P/P_s (P_s = 1.7 kPa) vs. the sensor output voltage, where P is measured with the 10 mmHg Baratron. It is used to determine the sensitivity of these sensors.

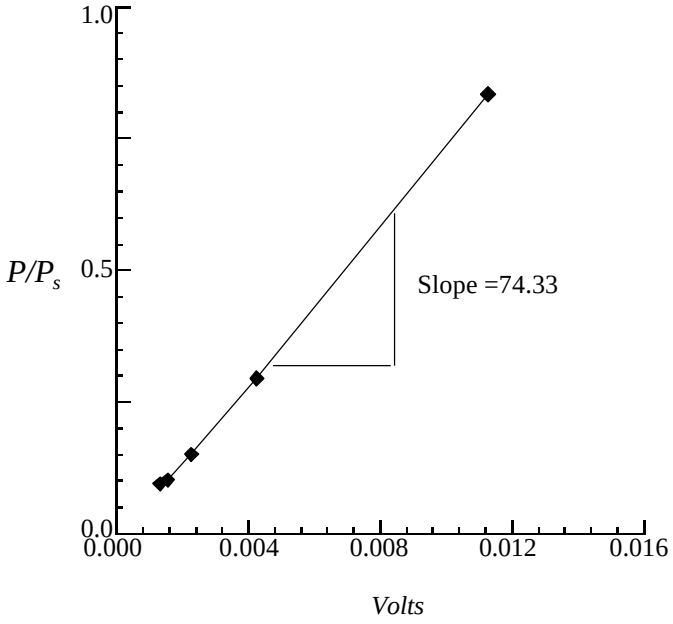

Figure 3.9 Calibration of the normalized pressure (Measured with the 10 mmHg Baratron) vs. voltage readings from the SenSym pressure sensor in the center at L/D = 0.726, 1.45, 2.18, 2.9, and 3.64 for U_o = 53.5 m/s (P_s = 1.7 kPa) (◆).

CHAPTER 4

CHARACTERIZATION OF THE BASELINE FLOW

4.1 Radial Velocity Distributions

The annular-return flow is investigated in the absence of actuation when the peak primary jet speed is $U_o = 53.5 \pm 1$ m/s ($Re_d = 3.12 \times 10^4$) and 26 ± 0.5 m/s ($Re_d = 1.50 \times 10^4$). Velocity distributions in the r-x^* plane are measured using PIV for L = 51 mm, 102 mm, 152 mm, and 255 mm. The data are taken over a 61 x 62 grid with a spot size of 32 x 32 pixels (73.4 μm/pixel). All measurements of the baseline flow field are conducted with a spatial resolution of 73.4 μm/pixel and frame-pair time delays of 10 μs and 23 μs for U_o = 53.5 m/s and 26 m/s, respectively. The velocity profile of the primary jet at the exit of the 8.9 mm tube is measured in a zoomed-in view (18.0 μm/ pixel) for a 53.5 m/s jet speed and time delay of 2 μs.

The cross-stream velocity distribution near the exit plane of the primary jet is shown in Figure 4.1 at $x^*/d = 0.08$ for L = 152 mm and U_o = 53.5 m/s. The velocity distribution is typical of a fully developed turbulent pipe flow with reasonable agreement to a power law fit (n = 6.5). The magnitude of the axial RMS velocity fluctuations on the centerline is 1.9 m/s (in agreement with independent hot wire anemometry).

Radial cross-stream distributions of the time-averaged velocity vectors for equally-spaced streamwise positions (2.38 mm apart) within the annular-return flow field

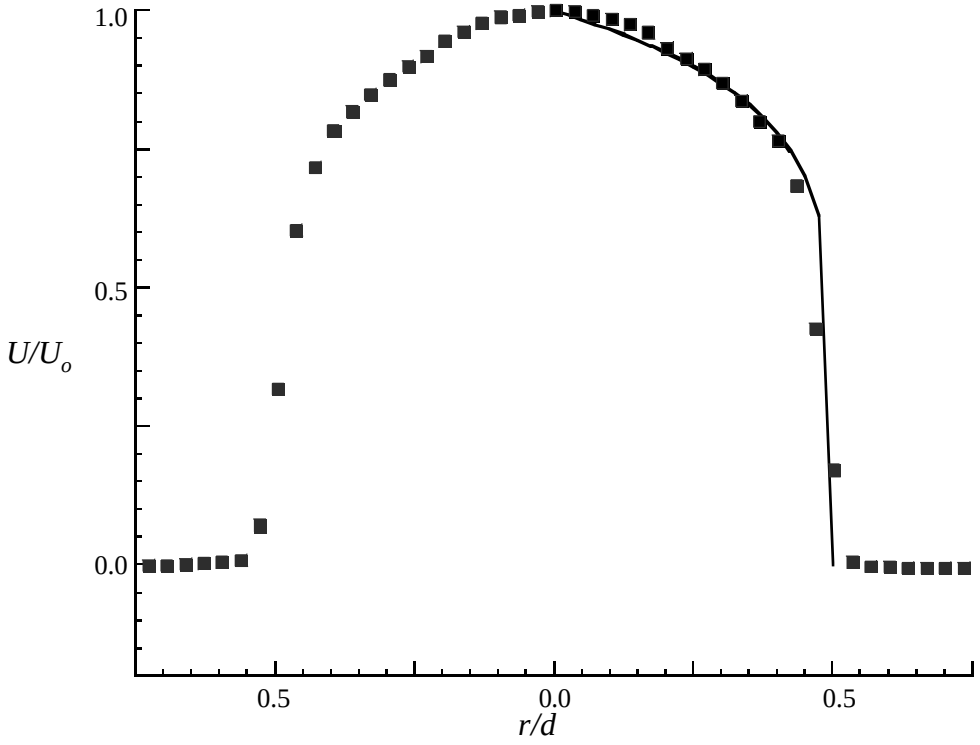

Figure 4.1 Streamwise velocity distribution in the primary jet at $x^*/d = 0$ for $Re_d = 3.12 \times 10^4$ and the Power law profile (n = 6.5) shown with a solid line.

are shown in Figures 4.2 & 4.3, where the velocity is normalized by the maximum centerline velocity for each test case (Table 4.1). For each configuration, the velocities in the center of the jet are substantially larger than those in the return flow (near the exit plane of the center tube) owing to the large area ratio (1:62.1) between the two domains.

Table 4.1 Maximum centerline velocities based on PIV data used for U_o in normalization and scaling calculations for the baseline flow.

Tube Length (L)	U_o = 53.5 m/s	U_o = 26 m/s
51 mm	53.3 m/s	26.1 m/s
102 mm	52.9 m/s	26.5 m/s
152 mm	54.4 m/s	26 m/s
255 mm	53.1 m/s	26.2 m/s

In Figures 4.2 & 4.3, solid lines are used to indicate contours of $U = 0$, which are taken to indicate the boundary between the jet and the return flow. These contours suggest that the radial spreading of the primary jet has three flow regimes; linear spreading, a transition zone and a regime for which the contour $U = 0$ varies only slightly near the end-wall. For L = 51 mm (L/D = 0.725 Figures 4.2a and 4.3a for U_o = 53.5 m/s and 26 m/s, respectively), the jet width increases linearly with x^*/D in the domain $0.0 < x^*/D < 0.1$ until it reaches a width of $r/D = 0.3$. The jet continues to spread linearly at a much lower rate in the domain $0.3 < x^*/D < 0.725$. A toroidal recirculation domain forms in the region bounded by $0.2 < x^*/D < 0.725$ and $0.2 < r/D < 0.5$. Note that the potential core of the primary jet ($0.0 < x^*/D < 0.6$) is in the same axial domain as the toroidal recirculation region.

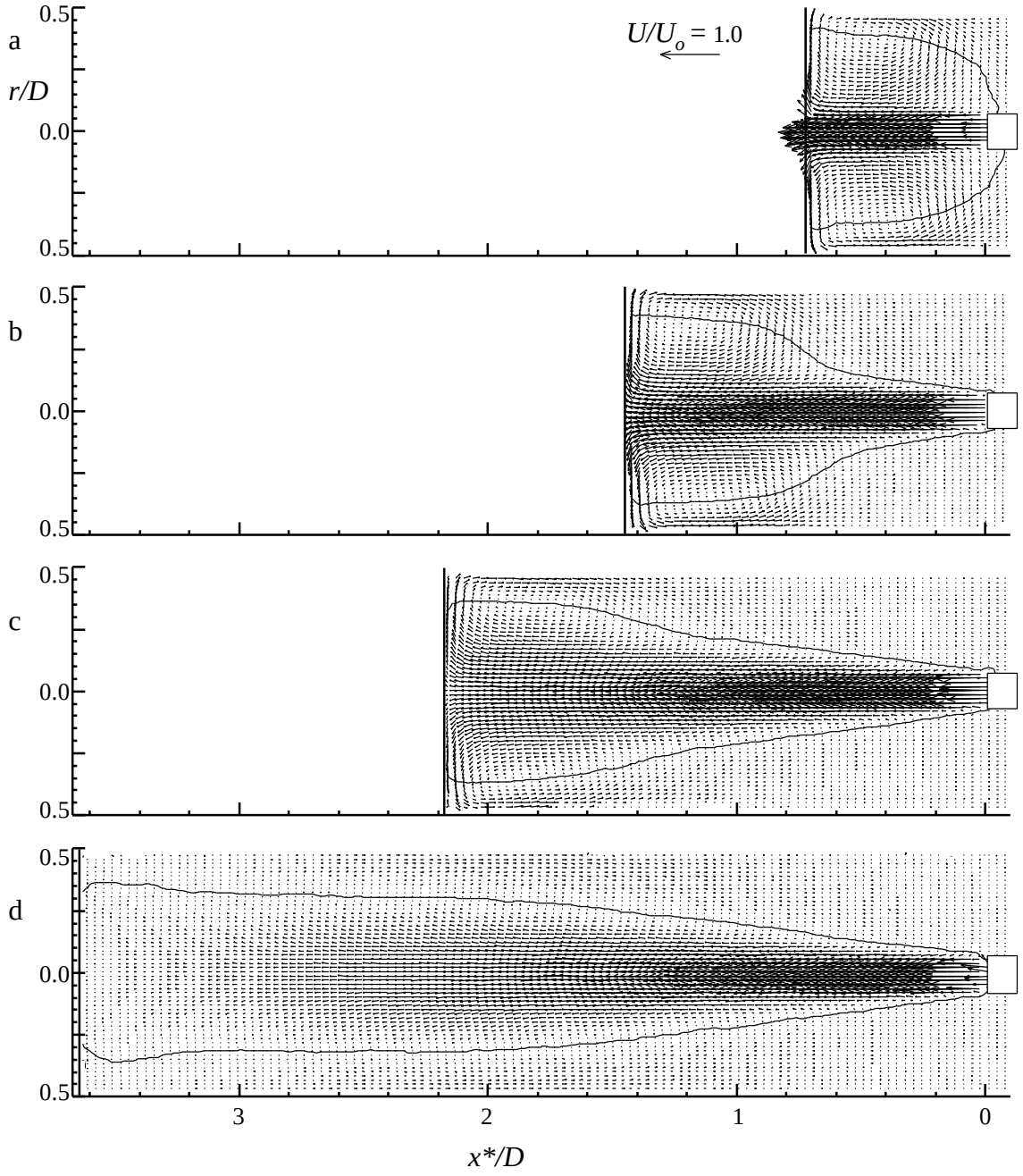

Figure 4.2 Radial distributions of the normalized time-averaged velocity vectors throughout the entire flow domain and contours of $U = 0$, represented by thin black lines, for a primary jet speed of $U_o = 53.5$ m/s for $L = 51$ (a), 102 (b), 152 (c), and 255 (d) mm (corresponding to $L/D = 0.726$ (a), 1.45 (b), 2.18 (c), and 3.64 (d), respectively). The end-wall positions are represented by vertical black lines.

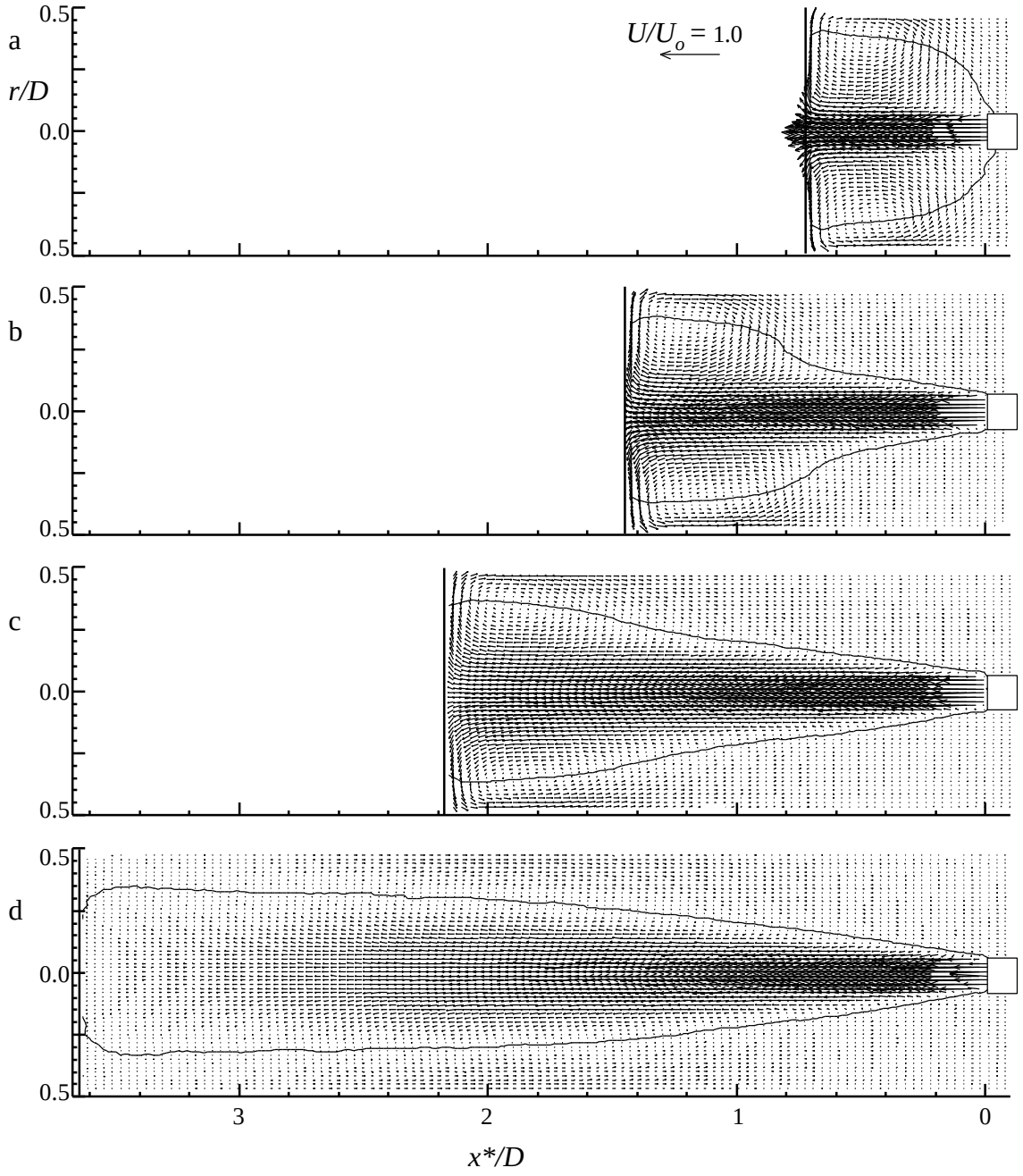

Figure 4.3 Radial distributions of the normalized time-averaged velocity vectors throughout the entire flow domain and contours of $U = 0$, represented by thin black lines, for a primary jet speed of U_o = 26 m/s for L = 51 (a), 102 (b), 152 (c), and 255 (d) mm (corresponding to L/D = 0.726 (a), 1.45 (b), 2.18 (c), and 3.64 (d), respectively). The end-wall positions are represented by vertical black lines.

When L = 102 mm (L/D = 1.45 Figures 4.2b and 4.3b), the primary jet spreads linearly in three streamwise segments $x^*/D < 0.6$, $0.6 < x^*/D < 0.9$ and $x^*/D > 0.9$, for U_o = 53.5 m/s. The spreading angle in the segment $x^*/D < 0.6$ is 8.8^o. A transition zone is observed in the segment $0.6 < x^*/D < 0.9$, where the jet spreads quickly, reaching a width of r/D = 0.33, and then continues spreading slowly in the segment $x^*/D > 0.9$. It appears that the spreading for 26 m/s is not linear in the segment $0.6 < x^*/D < 0.9$ as shown in Figures 4.3b. Within the transition domain, the rate of spreading of the contour $U = 0$ initially increases and subsequently decreases in an asymptotic manner until the width is given by r/D = 0.31. The jet then spreads linearly at slow rate in the segment $x^*/D > 0.9$. It is also evident that a toroidal recirculation domain exists in the domain bounded by $0.8 < x^*/D < 1.45$ and $0.2 < r/D < 0.5$.

The data for L = 152 mm (L/D = 2.18 Figures 4.2c and 4.3c) shows that the primary jet spreads in a linear manner with a spreading angle of 7.9^o in the domain $x^*/D < 1.0$. The transition zone, where the width increase to r/D = 0.34 with a slightly steeper slope, is visible in the domain $1.0 < x^*/D < 1.6$ as shown in Figures 4.2c and 4.3c. In Figures 4.2c and 4.3c, the contour $U = 0$ increases linearly with a very small slope within the domain $x^*/D > 1.6$, and the toroidal recirculation domain is located in the region bounded by $1.5 < x^*/D < 2.18$ and $0.2 < r/D < 0.5$. A magnification showing this toroidal recirculation domain is shown in Figure 4.4 ($1.7 < x^*/D < 2.2$ and $0.0 < r/D < 0.5$). Figure 4.4 shows a stagnation point flow near the end-wall ($2.1 < x^*/D < 2.18$ and $0.0 < r/D < 0.25$) and a toroidal recirculation domain in the region $1.7 < x^*/D < 2.18$ and $0.25 < r/D < 0.5$.

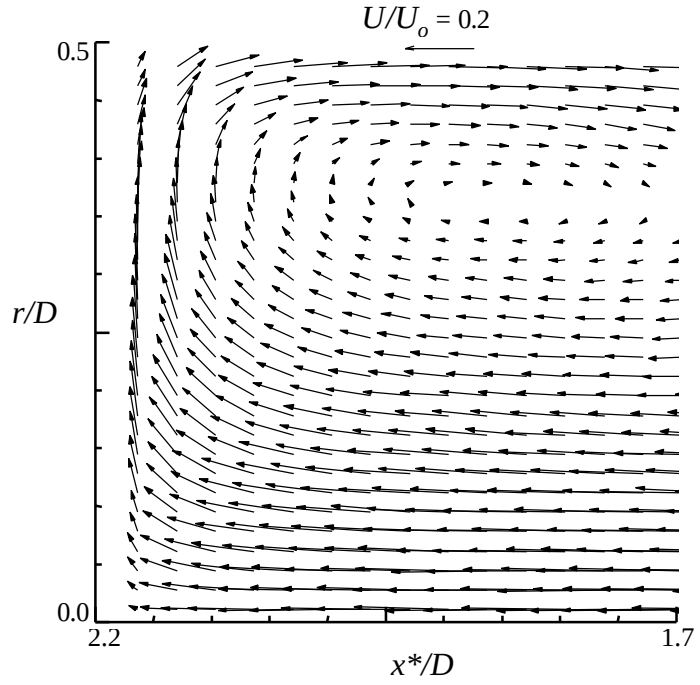

Figure 4.4 Magnified view of the stagnation region at the end-wall showing the normalized mean velocity vectors for the test case L = 152 mm and U_o = 53.5 m/s.

Finally, the data for L = 255 mm (L/D = 3.64 Figures 4.2d and 4.3d) show that the primary jet spreads linearly with a spreading angle of 7.0^o, as the contour U = 0 increase to r/D = 0.27 at x^*/D < 1.8. Subsequently, the width of the jet increases linearly with a very small slope in the domain x^*/D > 1.8. It is noteworthy that no distinct toroidal recirculation domain is observed for L = 255 mm. While Eckmann et al. (1996) suggest that the recirculation domain should span the entire flow domain, it is hard to distinguish between regular jet entrainment and the long recirculation domain in the entire flow field. The slight fluctuations seen in U = 0 at x^*/D > 1.8 are due to the fact that the velocities near U = 0 are very small and are not well resolved with the global PIV time delay

(10 μs). Furthermore, optical distortions, resulting from the circular geometry of the annular tube, may also have contributed to this anomaly.

Based on the description of the data given above, it may be concluded that the change in the cross-stream spreading of the jet is associated with the formation of the toroidal recirculation domain. The term transition zone refers to the streamwise segment for which the rate of spreading increases downstream of the initial linear spreading. This transition zone corresponds to the region in which the toroidal recirculation domain injects fluid into the primary jet, dramatically increasing the mass flux in the streamwise direction. Furthemore, the domains associated with the transition zone move closer to the exit plane as L decreases.

The nominal half-spreading angle of a round turbulent jet (based on half the centerline velocity) is 5.5^o (Rajaratnam, 1976). The present data shows that for L = 255, 152, and 102 mm the half-spreading angles of the jet in the dead-end annular-return flow are 2.7^o, 1.7^o, and 0.6^o, respectively. The half-spreading angle of the jet decreases with L, ostensibly because the interaction between the jet and the countercurrent return flow balances the spreading of the jet. On the other hand, the present data also shows that as L decreases, the rate of spreading of the contour U = 0 increases, due to the stronger interaction with the countercurrent return flow. The width of the region associated with low velocities increases as L decreases, suggesting that the rate at which the exhaust fluid is entrained per unit streamwise length increases along the positive x^* direction. Therefore, L/D has a significant impact on the rate of exhaust recirculation by its effect on the structure of the primary jet and the location and intensity of the toroidal recirculation domain.

For each position of the end-plug, the general shape of the contour of $U = 0$ is reasonably similar for the two Reynolds numbers tested here, except perhaps for $L = 51$ mm. This may be attributed to the presence of the toroidal recirculation domain, whose width is comparable to the test section radius ($R = 35$ mm). Furthermore, for this tube length the fluid in the toroidal recirculation domain interacts with the potential core and therefore alters the overall velocity profile of the main jet. The insensitivity of the contour of $U = 0$ for the two Reynolds numbers tested here is consistent with the predictions proposed by Abramovich (1963). His work indicates that the contour of zero axial velocity is only a function of b_o, R and x^*.

The data in Figures 4.1, 4.2, 4.3, and 4.4 are based on the time-averaged flow in the dead-end tube. However, it is clear that the instantaneous flow is not axisymmetric, particularly near the end-wall. The stagnation point continuously migrates about the centerline. An example of these flow patterns is shown in Figure 4.5, which shows evidence of radial "flapping" motions of the jet and return flows. In fact, these instabilities are important in mixing (or reactor) applications and can, potentially, be induced and manipulated by radial actuation as discussed in more detail in chapter 5. Figure 4.5 shows a substantial distortion of the secondary, toroidal recirculating flow domain below the centerline, and the corresponding changes in the return flow above the centerline. The stagnation point appears to move well below the centerline (and most likely out of the measurement plane).

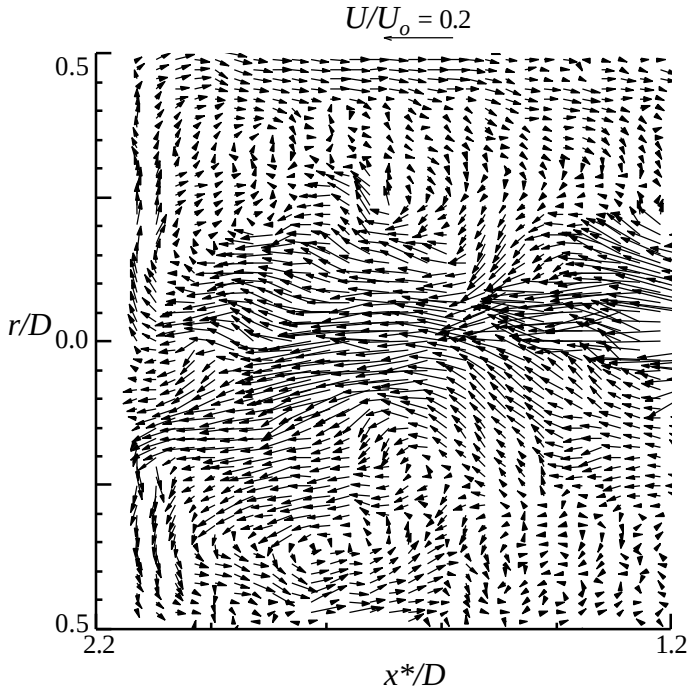

Figure 4.5 Sample of the normalized instantaneous velocity vector fields near the end-wall.

4.2 Centerline Velocity

The streamwise variation of the centerline velocity (U_m), normalized by the maximum centerline velocity (Table 4.1), is shown in Figures 4.6a and 4.6b for U_o = 53.5 m/s and 26 m/s, respectively with superimposed curve fits. Figures 4.6a and 4.6b show the evolution of two distinct flow regimes. In the domain $0.0 < x^*/D < 0.5$ ($0.0 < x^*/d < 3.9$), the effects of the shear layer between the jet and the countercurrent flow are minimal for all values of L (similar to the potential core in conventional round jets) and the centerline velocity decreases by less than 10%. This region is somewhat smaller than that given by Hrycak, et al. (1970), who reported a jet core of approximately $6d$ for turbulent impinging jets with $Re_d > 4000$.

As shown in Figures 4.6a and 4.6b, for $x^*/D > 0.5$ the centerline velocity decays very rapidly as the jet reaches the end-wall. In general the decay of the centerline velocity may be described by the expression $x^{*\,-1.2}$, shown as a solid line in Figures 4.6a and 4.6b, as compared to $x^{*\,-1}$ (dotted line Figure 4.6b) given by Rajaratnam (1976) for a free turbulent jet. Hence, the jet is clearly affected by the countercurrent flow. Furthermore, the similarity between the data for the two Reynolds numbers is quite remarkable. A comparison with the centerline velocities calculated using the analytical model proposed by Abramovich (1963) is also shown in Figure 4.6a (using a dashed line) for $x^*/D < 2.0$. The equations derived by Abramovich (equations 1 and 2 in chapter 2) characterize the decay of the centerline velocity in the domain $0.5 < x^*/D < 2$ for an infinitely long dead-end tube. It is remarkable that the centerline velocity calculated using Abramovich's solution is slightly higher than the measured values for $0.5 < x^*/D < 1.0$.

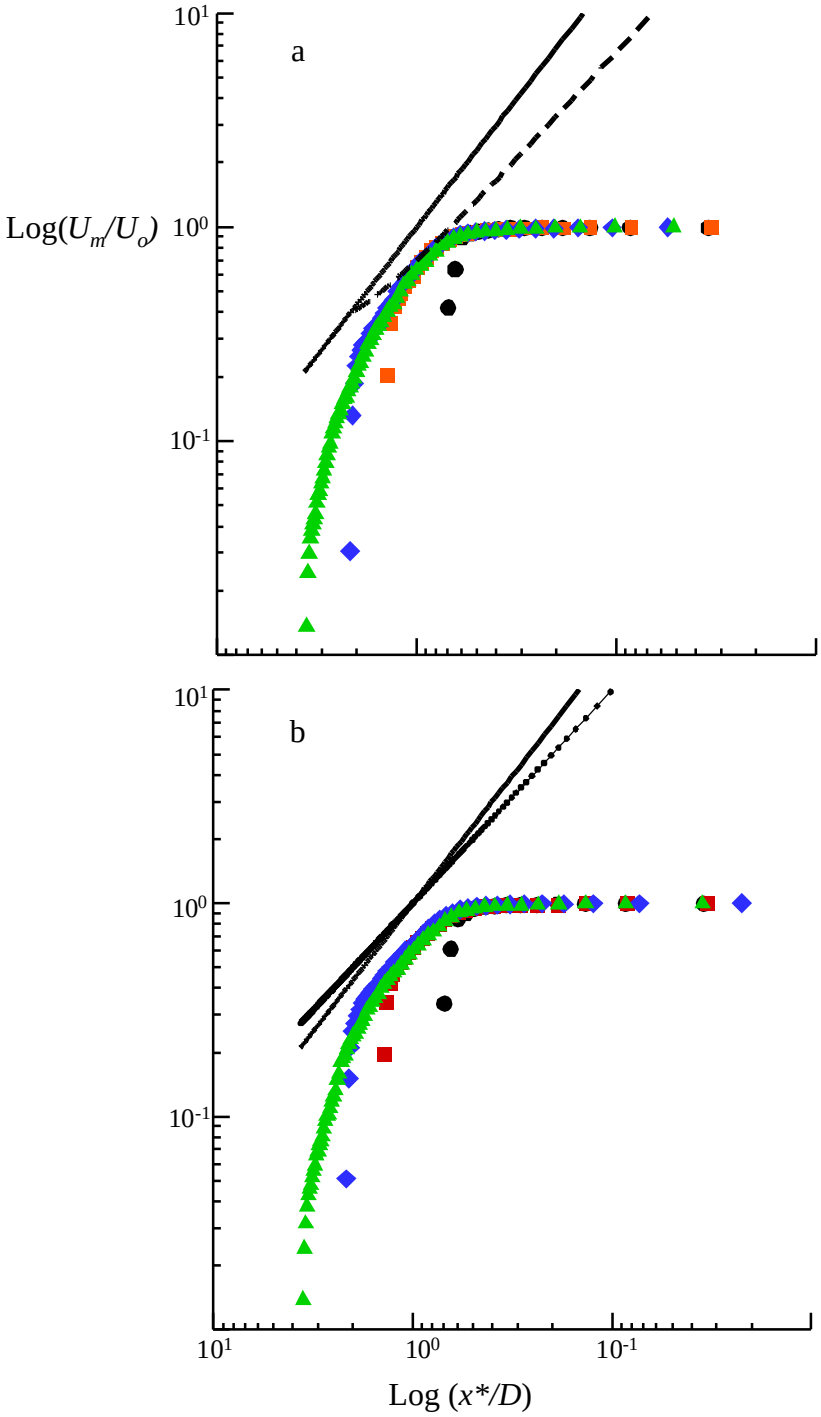

Figure 4.6 Variation of the centerline velocity for U_o = 53.5 m/s (a) and U_o = 26 m/s (b) for L = 51 (●), 102 (■), 152 (◆), and 255 (▲) mm (L/D = 0.726, 1.45, 2.18, and 3.64, respectively), $(x^*)^{-1.2}$ (Solid line), Analytical Model (Abramovich, 1963)(--), and $(x^*)^{-1}$ (dotted line).

However, Abramovich's solution exceeds the experimental values by as much as 20 – 50% for $x^*/D > 1.0$. This discrepancy is probably caused by the absence of viscous losses in Abramovich's analysis.

4.3 Mass and Momentum Balance

The variation of the time-averaged, normalized axial mass flux (G/G_o) and momentum flux M/M_o with x^*/D for the streamwise flow ($U(r/D) > 0$) and return flow ($U(r/D) < 0$) for U_o = 53.5 m/s are shown in Figures 4.7 & 4.8 for L = 255 and 102 mm, respectively. The values of the mass flux ($G = ?\,rUrpdr$) and momentum flux ($M = ?\,rU^2rpdr$) are determined separately for the streamwise flow, between the centerline and $U = 0$ [$0 < r < r(U = 0)$]; and the return flow, between $U = 0$ and the annular wall [$r(U = 0) < r < 0.5D$]. In these data, G_o and M_o are the mass and momentum fluxes of the primary jet at the exit plane. These values are computed assuming that the velocity distribution of the primary jet at its inlet plane is given by the power law for a fully developed turbulent flow with n = 6.5. The centerline velocity is taken to be the peak axial velocity determined from the PIV data (Table 4.1).

A dead end flow configuration requires that the mass flux through the annular region at each streamwise position is equal to the mass flux in the jet direction. Although the match between the axial and return flow is quite good, there are some noteworthy discrepancies in the mass fluxes. For L = 255 mm (Figure 4.7a), G for the

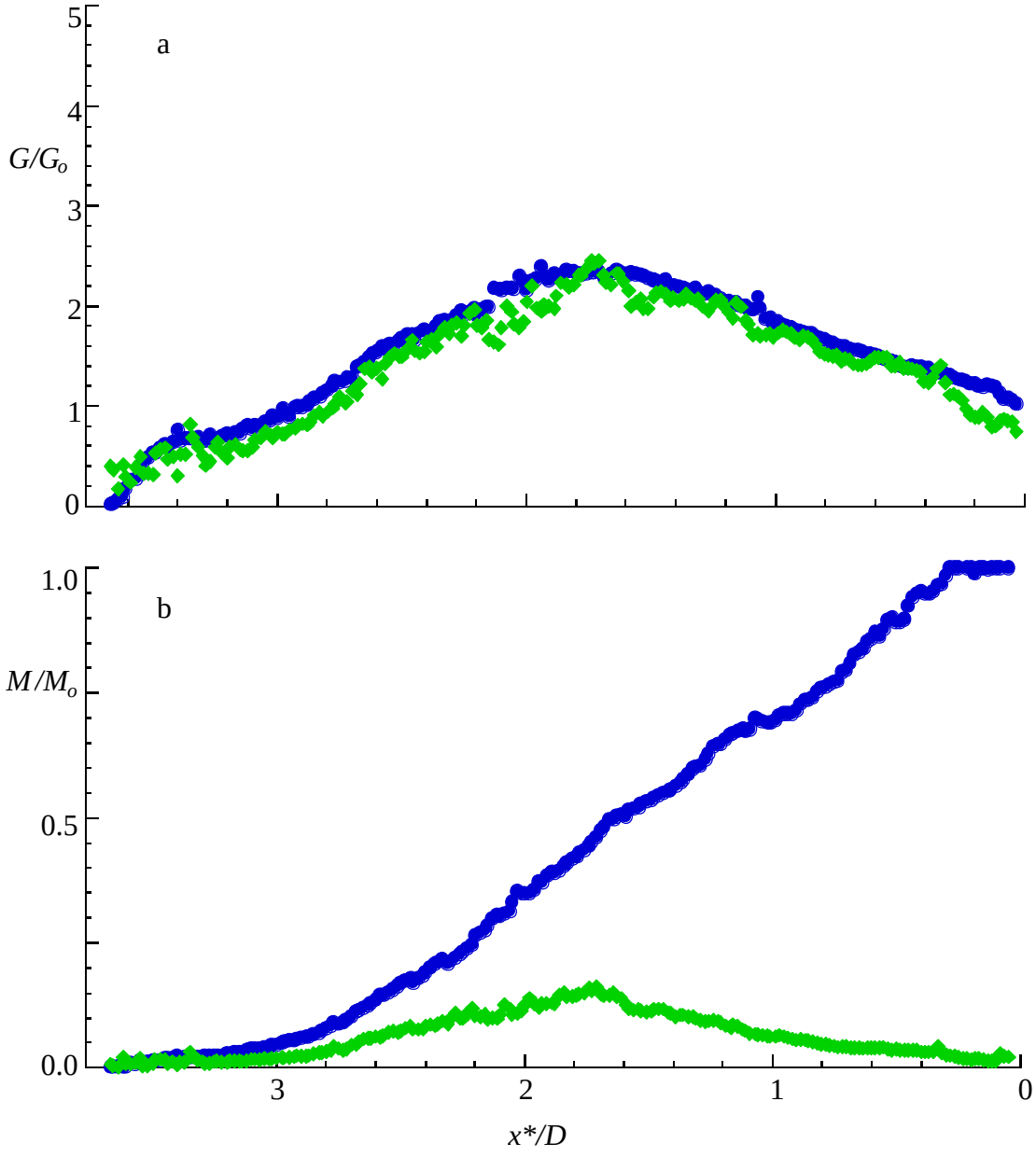

Figure 4.7 The mass flux (a) and the absolute value of the axial momentum flux (b) as a function of x^*/D for the primary jet (●) and the return flow (◆) for U_o = 53.5 m/s and L = 255 mm (L/D = 3.64).

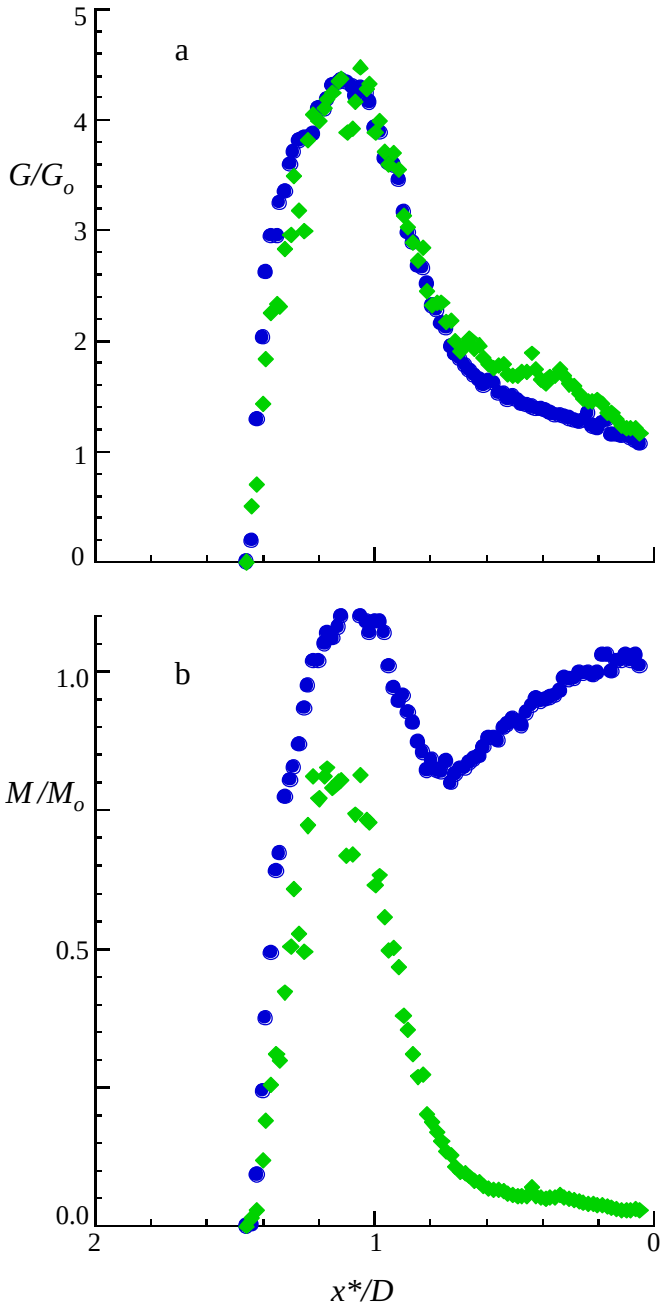

Figure 4.8 The mass flux (a) and the absolute value of the axial momentum flux (b) as a function of x^*/D for the primary jet (●) and the return flow (♦) for U_o = 53.5 m/s and L = 102 mm (L/D = 1.45).

return flow (♦) is lower than G in the streamwise direction (●) in the region $0 < x^*/D <$ 0.4. The reason is that the velocities within the return flow in this domain are very small, and are not well resolved with the global PIV time delay (10 μs). For L = 102 mm (Figure 4.8a), G in the return flow (♦) is higher than in the streamwise direction (●) in the domain $0.2 < x^*/D <0.7$, as a result of some asymmetry in the flow field and optical distortions, caused by the circular geometry of the annular tube.

For L = 255 mm, G/G_o in the streamwise flow (●) (Figure 4.7a) increases linearly with x^*/D from G/G_o = 1.00 to a maximum of G/G_o = 2.36 at x^*/D = 1.7. The increase in the streamwise mass flux occurs as the primary jet spreads and entrains fluid from the annular-return region ($0.15 < r/D < 0.5$) in the domain $0 < x^*/D < 1.8$. G/G_o in the return flow (♦) also increases to 2.36 at x^*/D = 1.7. Finally, the values of G/G_o in the streamwise and return flows decrease almost linearly within the domain $1.8 < x^*/D <$ 3.64 as the flow reverses direction, reaching zero at x^*/D = 3.64 (L/D). These data indicate that the fluid from the return flow is recirculated into the primary jet via entrainment, as noted by Abramovich (1963). A measure of the rate of recirculation is given by $A = (G - G_o)/G_o$. Based on the discussion above, the maximum value of A is 1.36 at x^*/D = 1.7 for L = 255 mm. The analytical solution of Abramovich (1963) indicates that for d/D = 0.1 and d/D = 0.2, A = 3 and 1, respectively for an axisymmetric system. In the present investigation d/D = 0.127, and a linear interpolation of Abramovich's results suggests that for d/D = 0.127 the maximum value of A is 2.5, which is above the value obtained from the measurements.

For L = 102 mm, G/G_o in the streamwise (●) and the return flow (◆) (Figure 4.8a) increases with x^*/D from 1.0 to 1.53 for $0.0 < x^*/D < 0.56$, followed by a sharp rise ($0.56 < x^*/D < 1.12$) to a peak level ($G/G_o = 4.36$) at $x^*/D = 1.12$, and a rapid decay to zero for $1.12 < x^*/D < 1.45$. For L = 102 mm, the maximum value of A is 3.36. It is noteworthy, that the streamwise position associated with the maximum value of G/G_o ($x^*/D = 1.12$) occurs within the domain associated with the toroidal recirculation domain (of Figures 4.2b & 4.3b). Calculations show that for L = 152 mm the maximum value of G/G_o is 3.94 (not shown in figures) and A = 2.94, which is greater than the value given by Abramovich for an infinitely long dead-end tube. It may be that the rate of flow recirculation between the primary jet and return flow increases with decreasing L/D.

As shown in Figure 4.7b, for L = 255 mm $M/M_o = 1$ for the streamwise flow at $0.0 < x^*/D < 0.15$. The value of M/M_o in the streamwise flow decays to zero for $0.15 < x^*/D < 3.64$. On the other hand, M/M_o in the return flow, which is small (approximately 0.05) compared to the streamwise flow, increases almost linearly with x^*/D to a maximum ($M/M_o = 0.15$) at $x^*/D = 1.7$. This increase follows the increase in G, and as the primary jet spreads, the cross-sectional area of the return flow decreases, causing an increase in the velocity of the return flow. Following the peak at $x^*/D = 1.7$, M/M_o in the return flow decreases for $1.7 < x^*/D < 3.64$ as G decreases in both the streamwise and return flow.

As shown in Figure 4.8b, for L = 102 mm M/M_o in the streamwise flow is approximately 1 for $0.0 < x^*/D < 0.15$ and then decays linearly to a local minimum at $x^*/D = 0.8$, followed by a sharp increase with increasing x^*/D to a maximum ($M/M_o = 1.1$) at $x^*/D = 1.1$. Likewise, M/M_o in the return flow reaches a maximum

(M/M_o = 0.85) at x^*/D = 1.2. The sharp increase of M in both the streamwise and return flows is caused by the presence of the strong toroidal recirculation domain $0.9 < x^*/D < 1.45$ (Figures 4.2b and 4.3b). In the domain, $0.8 < x^*/D < 1.1$ the toroidal recirculation domain injects a lot of fluid from the return flow into the primary jet. The sharp increase in mass flux (Figure 4.8a) for both the streamwise and the return flows results in an increase of the momentum flux for both the streamwise and return flows.

4.4 Velocity Fluctuations

The radial distributions of u' and v' scaled by the maximum centerline velocities (Table 4.1) are shown in Figures 4.9 & 4.10, respectively for U_o = 53.5 m/s and in Figures 4.11 and 4.12 for U_o = 26 m/s. These distributions show the evolution of the (nominally axisymmetric) primary jet shear layer and its cross-stream spreading into the return flow. The jet core is at $r/D < 0.06$ and the mixing layer at the periphery of the jet is in the region $0.06 < r/D < 0.15$ for $x^*/D < 0.65$. In the shear layer, u' and v' are significantly larger at the periphery of the jet ($0.04 < r/D < 0.15$) than u' and v' at the centerline ($r/D = 0$) for all test cases. The peak values of u' and v' (at $r/D = 0.06$) are approximately $0.24U_o$ and $0.07U_o$, respectively, and it is evident that the jet is spreading into the return flow. As the jet continues to spread, the peaks diminish and the radial distributions of u' and v' become reasonably smooth. The distributions of u' and v' show that for L = 51 mm the jet core retains its structure throughout the length of the tube, however, for larger L, mixing and smooth profiles are attained for $x^*/D > 1$.

As noted in connection with (Figure 4.5), large-scale oscillations play a major role in the streamwise evolution of u' and v'. The large-scale radial flapping of the primary jet drives a time dependant redistribution of the flow in the annular domain. At the same time, as x^*/D increases, the spreading of the primary jet reduces the effective cross-sectional area of the region occupied by the return flow, thereby intensifying the amplitude of the velocity fluctuations. In fact, the magnitude of u' and v' in the return

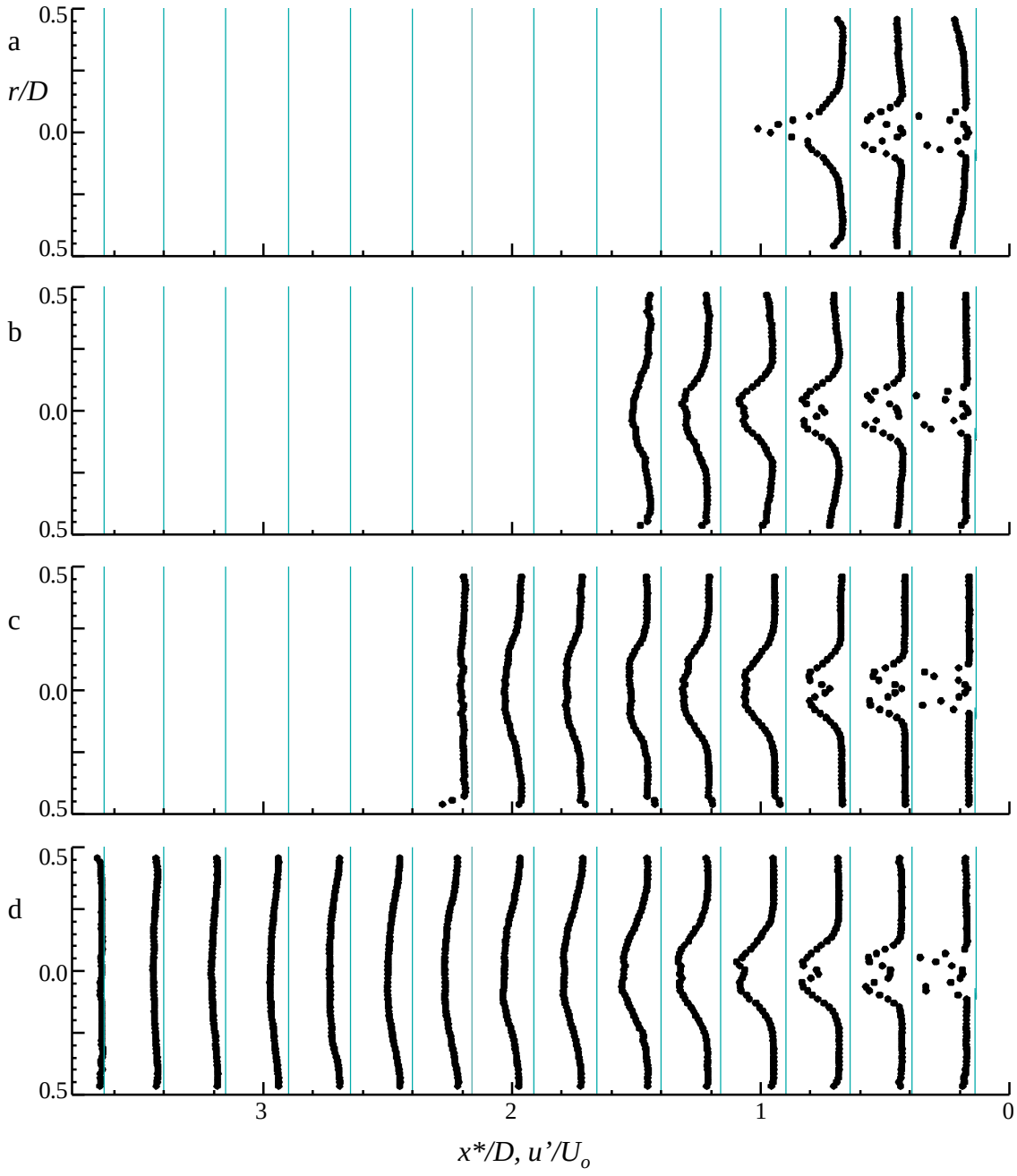

Figure 4.9 Radial distributions of *u'* for U_o = 53.5 m/s and L = 51 (a), 102 (b), 152 (c), and 255 (d) mm (corresponding to L/D = 0.726 (a), 1.45 (b), 2.18 (c), and 3.64 (d), respectively) in the domain $0.14 \leq x^*/D \leq 3.64$ at intervals of $0.25D$ marked by gray lines.

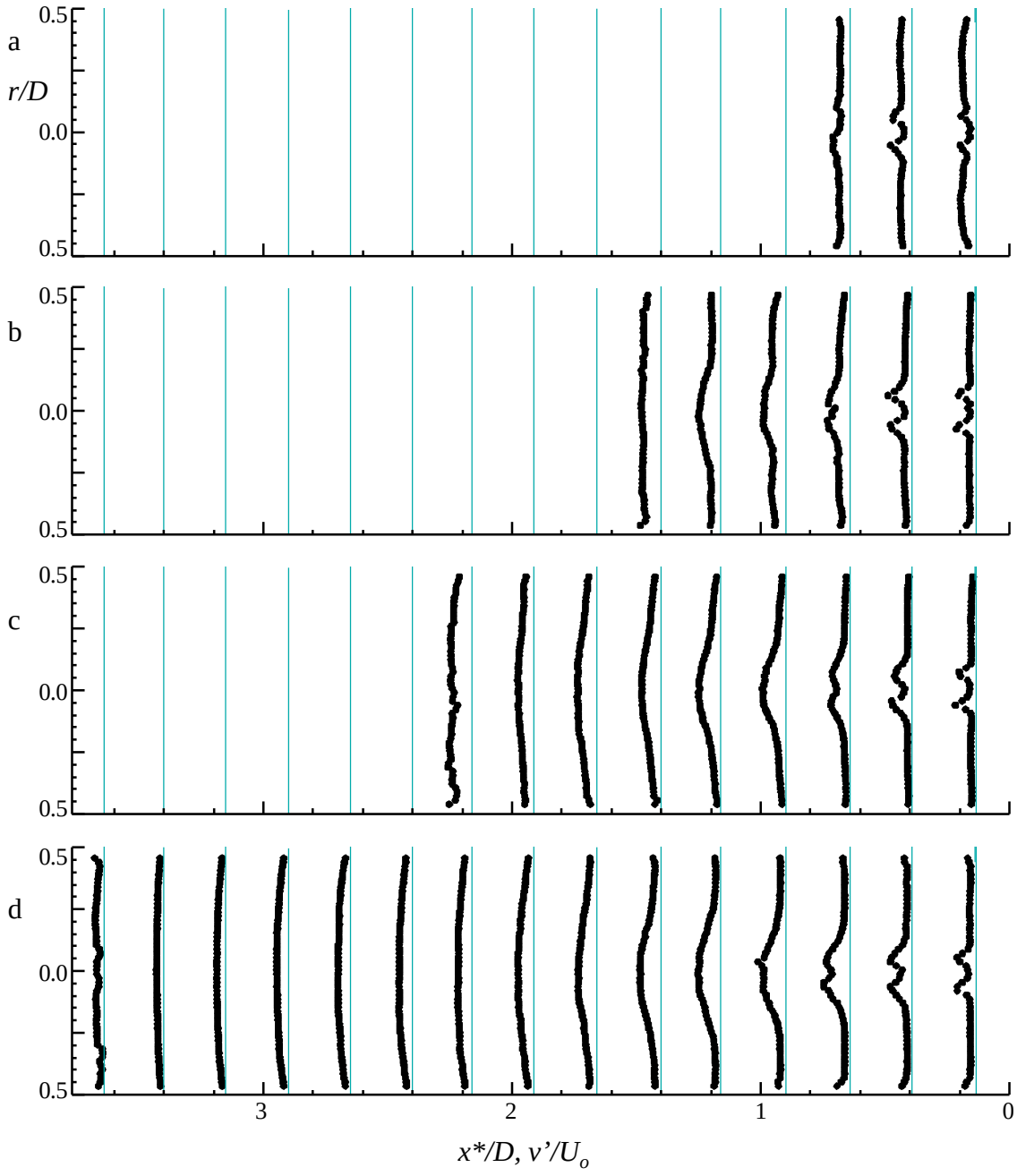

Figure 4.10 Radial distributions of v' for U_o = 53.5 m/s and L = 51 (a), 102 (b), 152 (c), and 255 (d) mm (corresponding to L/D = 0.726 (a), 1.45 (b), 2.18 (c), and 3.64 (d), respectively) in the domain $0.14 \leq x^*/D \leq 3.64$ at intervals of $0.25D$ marked by gray lines.

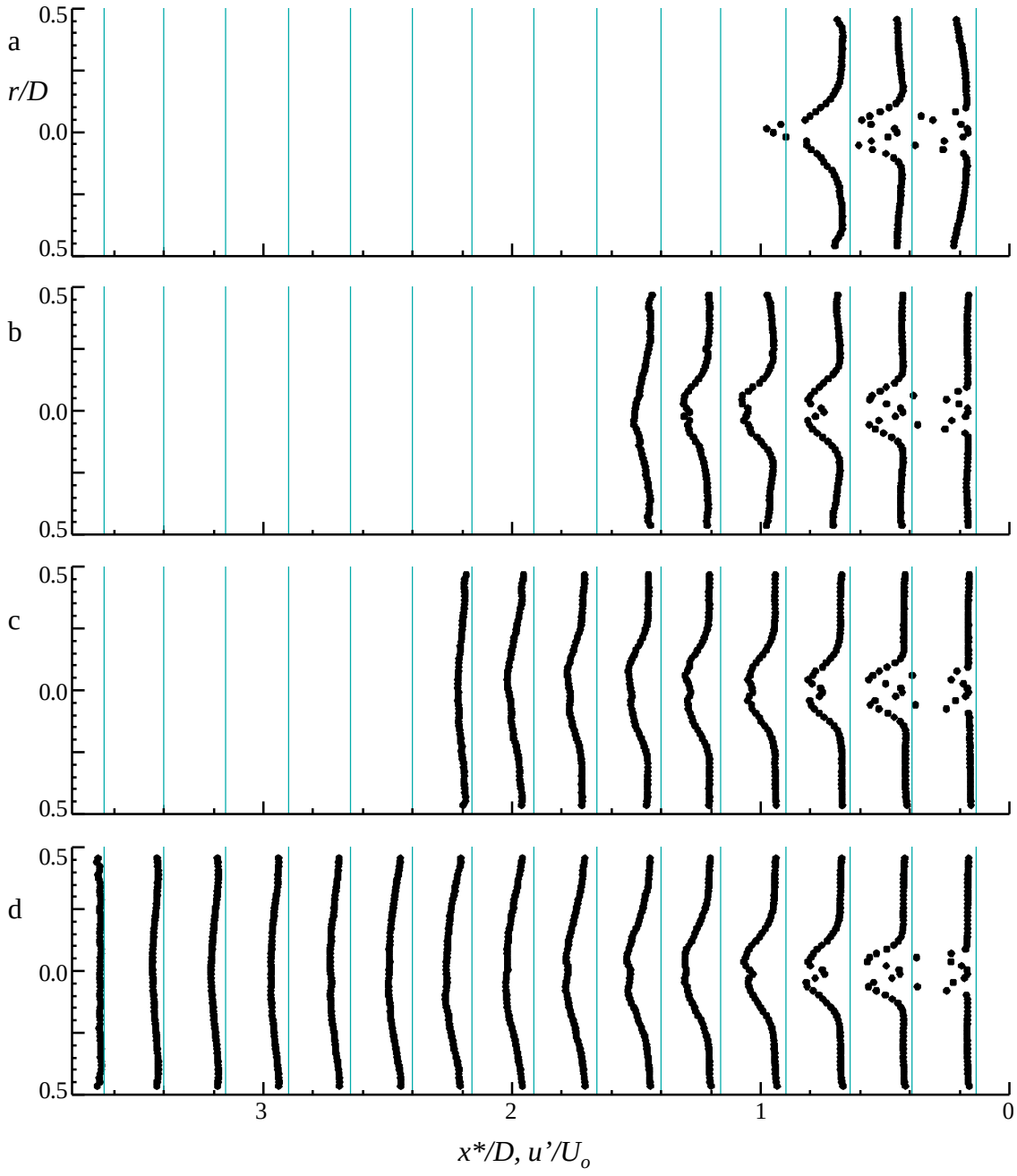

Figure 4.11 Radial distributions of u' for U_o = 26 m/s and L = 51 (a), 102 (b), 152 (c), and 255 (d) mm (corresponding to L/D = 0.726 (a), 1.45 (b), 2.18 (c), and 3.64 (d), respectively) in the domain $0.14 \leq x^*/D \leq 3.64$ at intervals of $0.25D$ marked by gray lines.

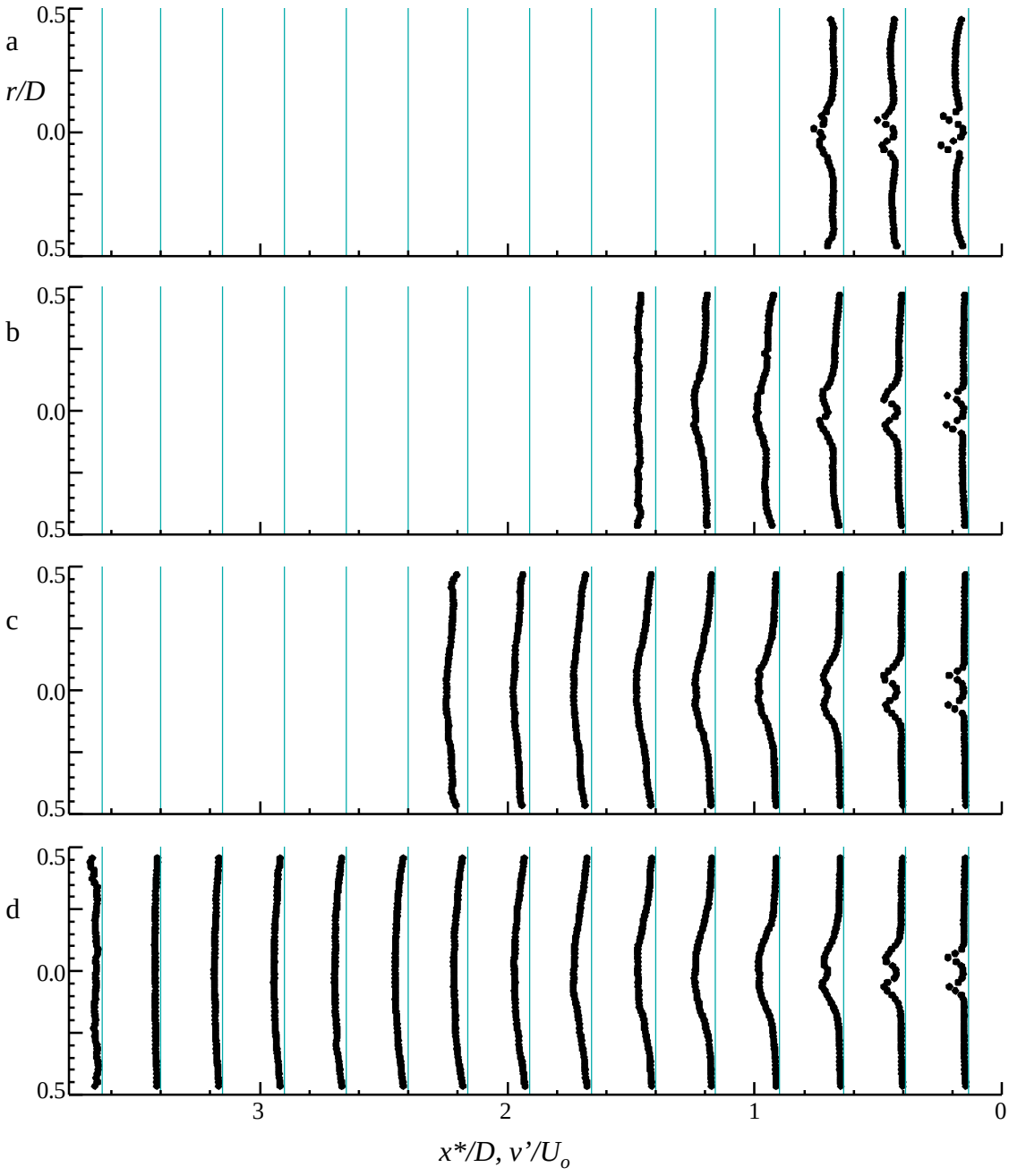

Figure 4.12 Radial distributions of v' for U_o = 26 m/s and L = 51 (a), 102 (b), 152 (c), and 255 (d) mm (corresponding to L/D = 0.726 (a), 1.45 (b), 2.18 (c), and 3.64 (d), respectively) in the domain $0.14 \leq x^*/D \leq 3.64$ at intervals of $0.25D$ marked by gray lines.

flow is on the order of the mean velocity there. It is also evident that the turning of the flow near the end-wall leads to some increase in *v'*. The distributions of *u'* and *v'* for U_o = 26 m/s (Figures 4.11 and 4.12) are very similar to the distribution in Figures 4.9 and 4.10. Note also that in the long tubes the cross-stream distributions of *u'* and *v'* are quite uniform and almost invariant with *x** at *x*/D* > 2.5 (Figures 4.9d and 4.10d). The fact that *v'* does not increase significantly at the end-wall (*x*/D* = 3.64 in Figures 4.9d and 4.10d) indicates a slow turning of the flow, as is also evident from the low levels of mass and momentum fluxes there.

4.5 Vorticity

Table 4.2 The maximum vorticity (W_o) for normalization and scaling calculations for the baseline flow.

Tube Length (*L*)	U_o = 53.5 m/s	U_o = 26 m/s
51 mm	21300/sec	11200/sec
102 mm	21400/sec	11800/sec
152 mm	22300/sec	11100/sec
255 mm	19900/sec	11300/sec

The radial distributions of the azimuthal vorticity *W* for U_o = 53.5 m/s and 26 m/s are shown in Figures 4.13 and 4.14, respectively. *W* is scaled by the maximum azimuthal vorticity W_o at *r/D* = 0.06 (Table 4.2). Figures 4.13a-d and 4.14a-d show that *W* is largest in the periphery of the jet. Of course, on the jet centerline the vorticity is zero and its

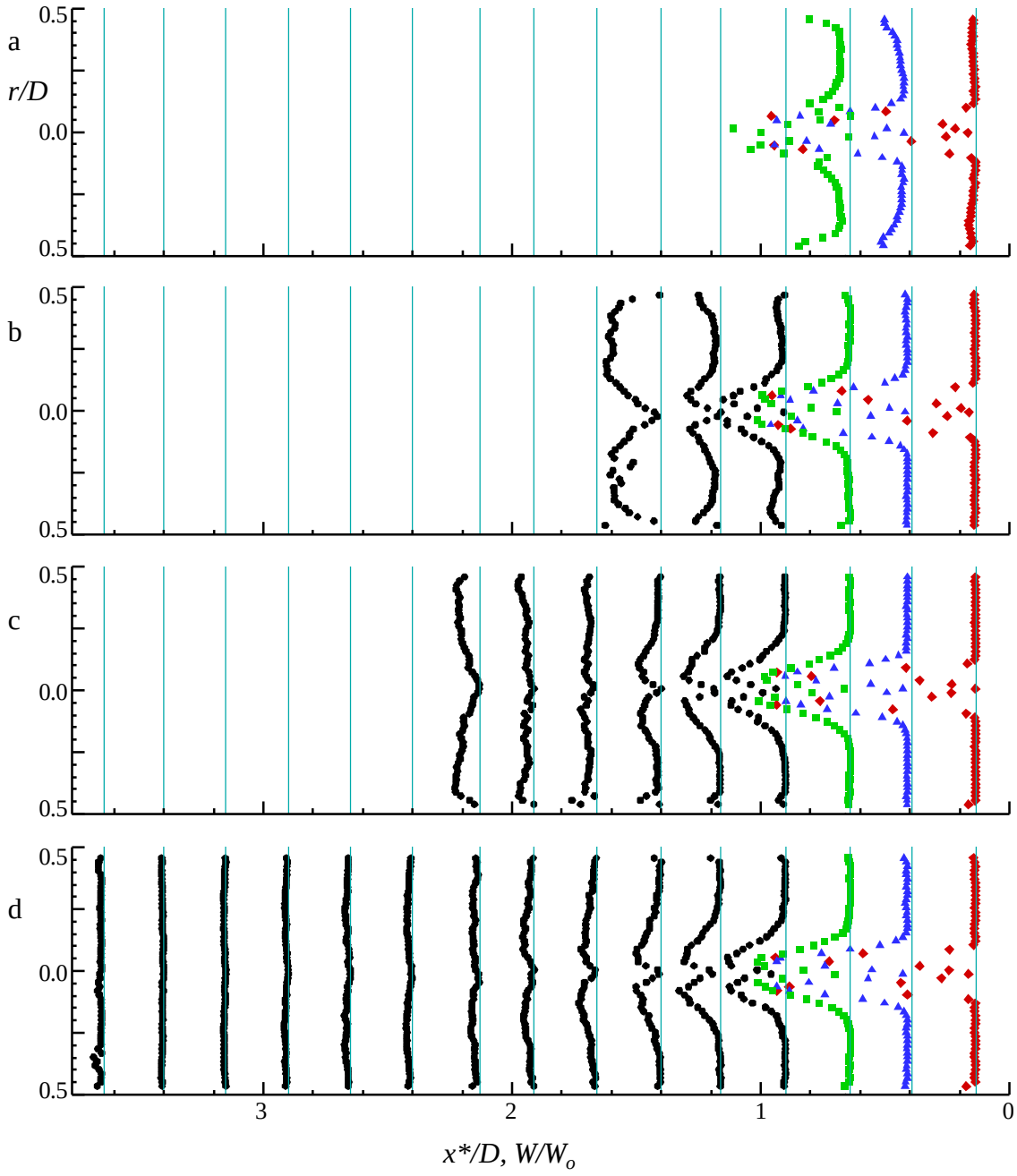

Figure 4.13 Radial distributions of the normalized vorticity (W/W_o) for U_o = 53.5 m/s and L = 51 (a), 102 (b), 152 (c), and 255 (d) mm (corresponding to L/D = 0.726 (a), 1.45 (b), 2.18 (c), and 3.64 (d), respectively) in the domain $0.14 \leq x^*/D \leq 3.64$ at intervals of $0.25D$ marked by gray lines. Different shapes and colors are used to differentiate profiles that overlap.

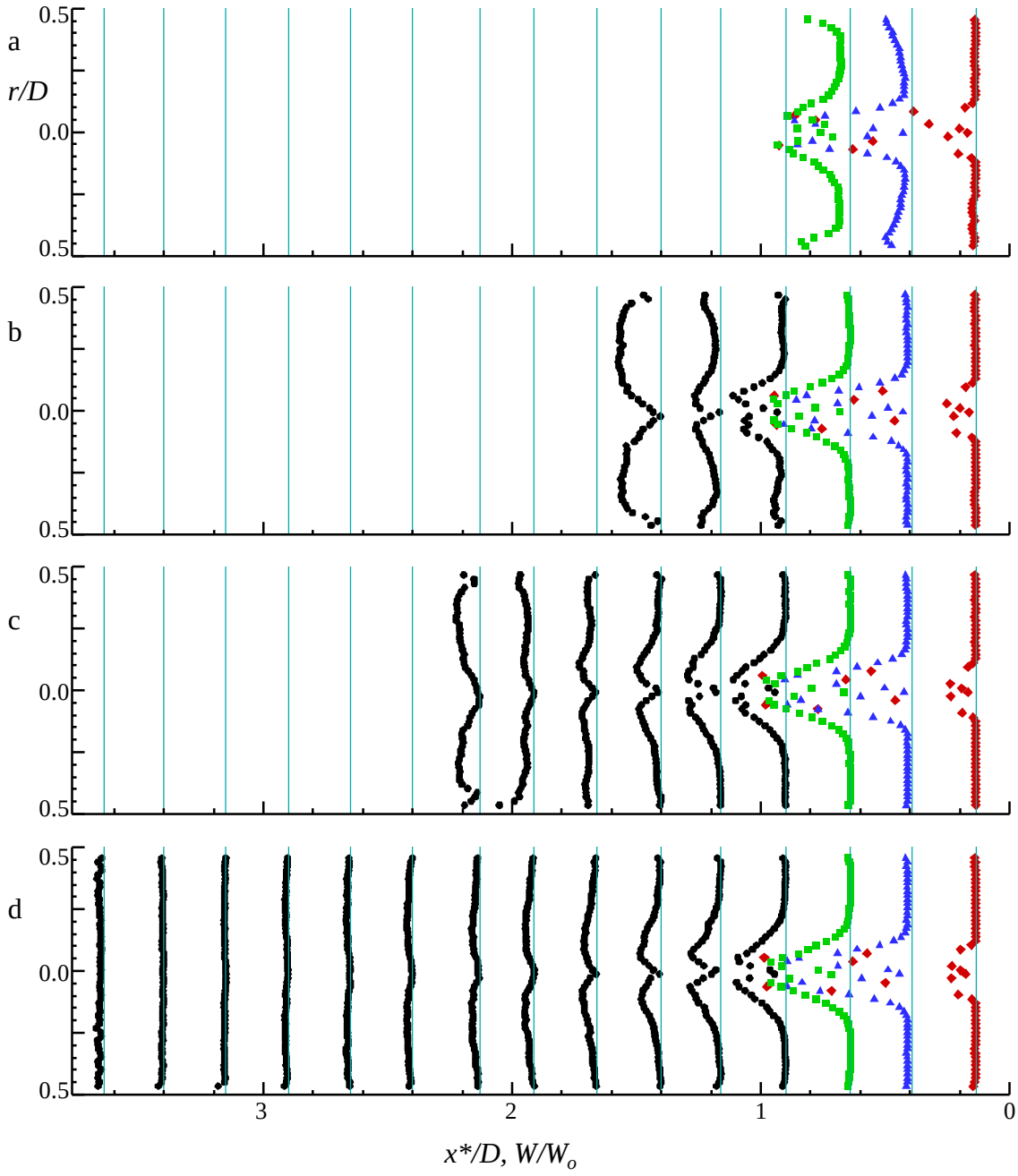

Figure 4.14 Radial distributions of the normalized vorticity (W/W_o) for U_o = 26 m/s and L = 51 (a), 102 (b), 152 (c), 255 (d) mm (corresponding to L/D = 0.726 (a), 1.45 (b), 2.18 (c), and 3.64 (d), respectively) in the domain $0.14 \leq x^*/D \leq 3.64$ at intervals of $0.25D$ marked by gray lines. Different shapes and colors are used to differentiate profiles that overlap.

sense is reversed. However, in the present plots, the sense of W on both sides of the centerline is ignored by plotting its absolute value. The jet ultimately spreads radially to form the recirculating flow domains of the return flow.

The turning of the flow near the end-wall for L = 51, 102, and 152 mm is evident in Figures 4.13a-c (L/D = 0.725, 1.45, and 2.18, respectively). These distributions are characterized by a minimum near the centerline and a local maximum between it and the outer shell. For L = 51mm, most of the flow turns at the end-wall and again at the annular surface forming a strong wall jet characterized by very high magnitudes of W near the end-wall ($0.4 < r/D < 0.47$). When L = 255 mm, the primary jet barely reaches the end-wall. In this case, most of the fluid turns backwards before reaching the end-wall, and the turning of the flow is much slower.

4.6 Pressure Along the End-Wall

The distributions of the mean pressure (P), normalized by the stagnation pressure of the primary jet (P_s) at $x^*/D = 0$, along the vertical and horizontal diametric lines on the end-wall are shown in Figures 4.15 and 4.16 for U_o = 53.5 m/s and 26 m/s, respectively. In the pressure distributions for L = 51, 102, and 152 mm, the stagnation point is made evident by a maximum at the center of the end-wall ($r/D = 0$). The pressure decreases radially, reaching a local minimum at $r/D \sim 0.33$ and then increases slightly for $0.33 < r/D < 0.5$. The increase of the pressure near the annular surface is due to the stagnation of

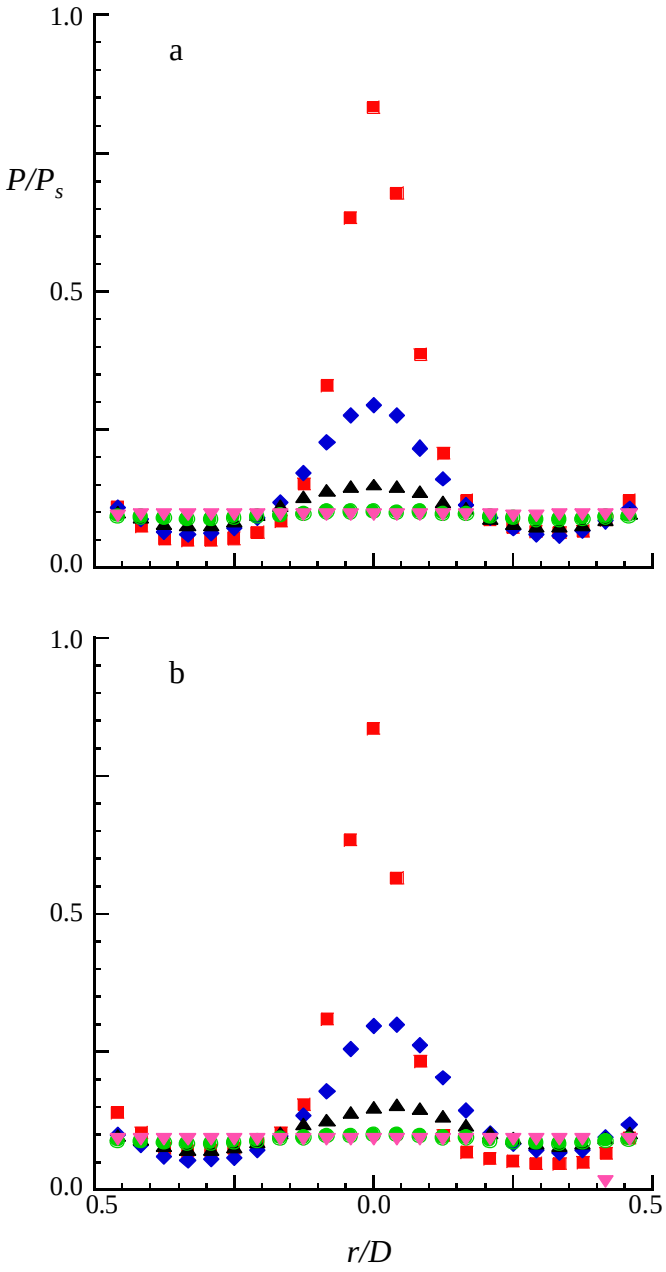

Figure 4.15 Radial distributions of the normalized mean pressure along the vertical (a) and horizontal (b) diametric lines of the end-wall for U_o = 53.5 m/s (P_s = 1.7 kPa) and L = 51 (■), 102 (◆), 152 (▲), 203 (●) and 255 (▼) mm (corresponding to L/D = 0.726, 1.45, 2.18, 2.9, and 3.64, respectively).

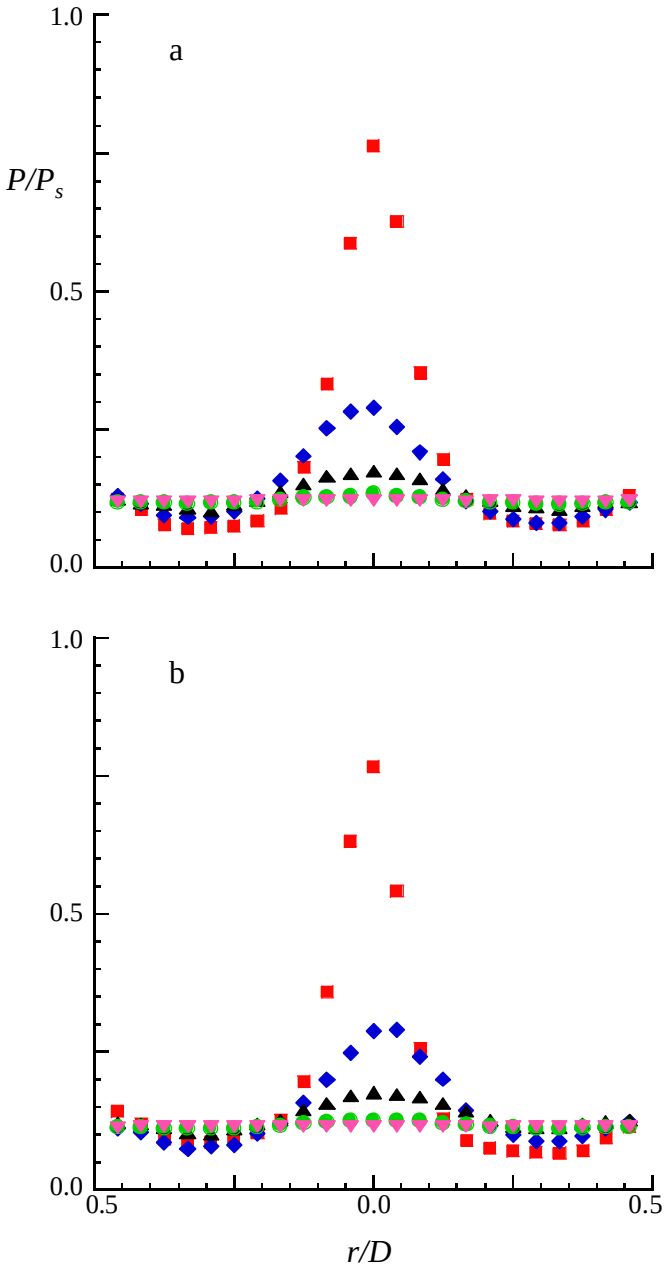

Figure 4.16 Radial distributions of the normalized mean pressure along the vertical (a) and horizontal (b) diametric lines of the end-wall for U_o = 26 m/s (P_s = 0.4 kPa) and L = 51 (■), 102 (◆), 152 (▲), 203 (●) and 255 (▼) mm (corresponding to L/D = 0.726, 1.45, 2.18, 2.9, and 3.64, respectively).

the flow at the annular surface. The same trends are also apparent for the pressure distribution along the horizontal diametric line (Figures 4.15b and 4.16b). These distributions show that for $L \leq 152$ mm the primary jet impinges on the end-wall, turns and forms a radial wall jet, which slows down as it reaches the annular surface.

For L = 203 mm and 255 mm ($L/D \geq 2.9$), the radial pressure distributions are uniform across the entire end-wall (Figures 4.15a-b and 4.16a-b). This observation is in agreement with the results of the numerical simulation of Amano (1986), who reported that for every value of d/D, there is a value of L/D past which P is invariant along the end-wall (called the terminal stagnation pressure) with respect to the depth of the tube. The numerical calculations (Amano, 1986) indicate that for d/D = 0.125 the terminal stagnation pressure is approximately $0.07P_s$ at L/D = 2.9, but the pressure continues to decay slightly after reaching this point. Hence, the current experimental results indicate that the terminal stagnation pressure $P \sim 0.1P_s$ is higher than the value indicated by the numerical simulations.

The mean pressure and its rms fluctuations (scaled by P_s) at r/D = 0 and r/D = 0.25 for L/D = 0.725, 1.45, 2.18, 2.9, and 3.64 (U_o = 53.5 m/s) are shown in Figures 4.17a and 4.17b, respectively. As shown in Figure 4.17a, for L/D = 0.725, P at r/D = 0.25 is slightly lower than the terminal stagnation pressure ($0.1P_s$) and increases asymptotically to the terminal stagnation pressure as the L/D increases to 3.64. The pressure for L/D = 0.725 is approximately $0.8P_s$ at r/D = 0 and its decrease is similar to the decrease of the stagnation pressure with L, as determined from the numerical simulations reported by Amano (1986). These data demonstrate that when d/D = 0.127 and $L/D < 2.2$, the flow field is characterized by full jet impingement and high amplitude fluctuations.

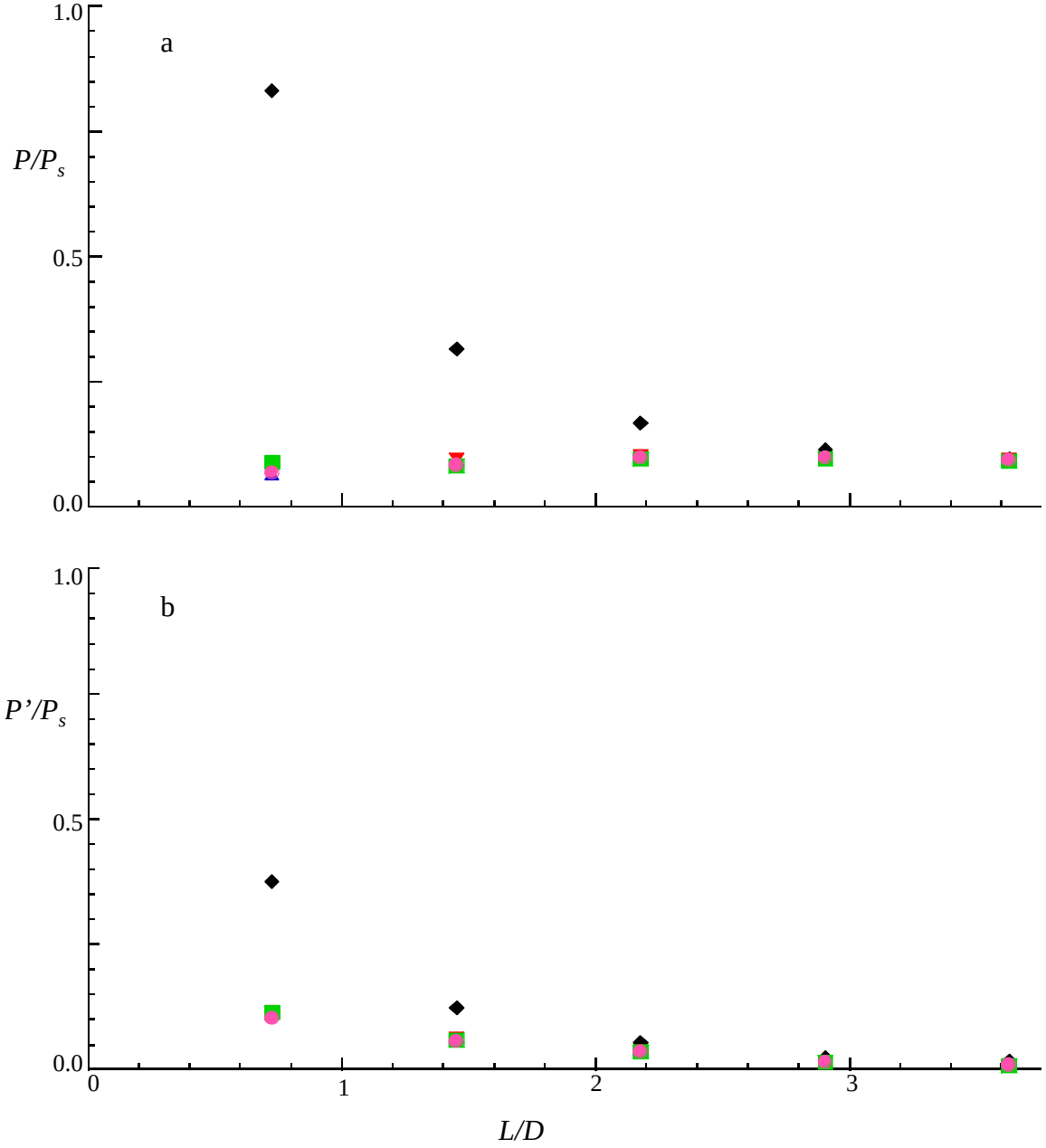

Figure 4.17 Variation of the normalized mean pressure (a) and rms pressure fluctuations (b) along the end-wall with L/D for U_o = 53.5 m/s (P_s = 1.7 kPa) at the center (◆) and r/D = 0.25 at ports #1 (▲), 2 (▼), 3 (■), and 4 (●).

CHAPTER 5

THE EFFECTS OF PULSED ACTUATION

In this chapter, the effects of pulsed actuation on the annular-return flow are investigated. Two pulsed-combustion actuators are used and are mounted diametrically opposite to each other immediately downstream of the primary jet (at x^*/d = 1.1). In the presence of a cross flow, the performance of each actuator is characterized in terms of the dimensionless momentum coefficient, which measures the ratio of momentum flux of the actuator to the primary jets (using the peak velocity of the jet, and density of air at STP).

$$C_m \equiv \frac{\left(\rho A V^2\right)_{actuator\ \ jet}}{\left(\rho A V^2\right)_{primary\ \ jet}}$$

As noted in Crittenden, et al. (2001), the instantaneous thrust/momentum of the actuator jet may be estimated from the pressure in the combustion chamber, assuming an isentropic expansion through the exhaust orifice. Since the momentum flux of the actuator jet varies over the (relatively short) duration of its pressure pulse, it is characterized in terms of both the average over the actuation cycle and the peak value, calculated from the pressure curve for stoichiometric hydrogen mixture (see Figure 2.5). For comparison, the momentum coefficient of the steady jet of gas from the actuator without ignition is also included. In the absence of ignition, C_m = 1.5 x10^{-3}. When the actuator is operated, the mean value over the cycle period is C_{mav} = 1.4 x10^{-2} (The instantaneous peak momentum coefficient value is C_m = 1.4).

5.1 Forcing with a Single Actuator

Some features of the interaction of the annular-return flow with a single actuator are shown in Figure 5.1. These data include the phased-averaged normalized velocity vectors with concentrations of the normalized azimuthal vorticity (W/W_o) and profiles of the normalized rms fluctuations of the axial and radial velocity components u' and v'. These phase-averaged data are obtained at equal time intervals (0.25 ms apart) after the ignition of the actuator. The repetition rate (10 Hz) of the actuator is sufficiently low to ensure that its transient effect on the flow can be fully assessed before the onset of the next pulse. The PIV data shown in Figures 5.1a-h are taken with a spatial resolution of 73.4 μm/pixel and frame-pair time delays of 10 μs. No data could be obtained in the actuator jet in the first several phases because it is not seeded.

At t = 0.27 ms (Figure 5.1a), the flow field exhibits the characteristics of the baseline flow. Subsequently, at t = 0.77ms (Figure 5.1b), the transient jet emanating from the actuator in the domain $0.1 < x^*/D < 0.2$ (below $r/D = 0$) impinges on the primary jet, and effectively acts as an obstruction. The primary jet flows around the impinging, transient jet, generating a wake like flow in $0.2 < x^*/D < 0.4$ and $0.0 < r/D < 0.15$, that is characterized by an increase in u' and v' at $x^*/D = 0.25$ for $0.0 < r/D < 0.15$. At t = 1.02 ms after ignition (Figure 5.1c), the transient jet completely penetrates through the primary jet and u' and v' attain very high values [$u' \sim O(0.35U_o)$ & $v' \sim O(0.45U_o)$] at $x^*/D = 0.25$ for $0.0 < r/D < 0.25$. At t = 1.27ms (Figure 5.1d), the transient jet deflects a large portion of the fluid in the primary jet toward the opposite wall ($r/D = 0.5$) and the remaining fluid

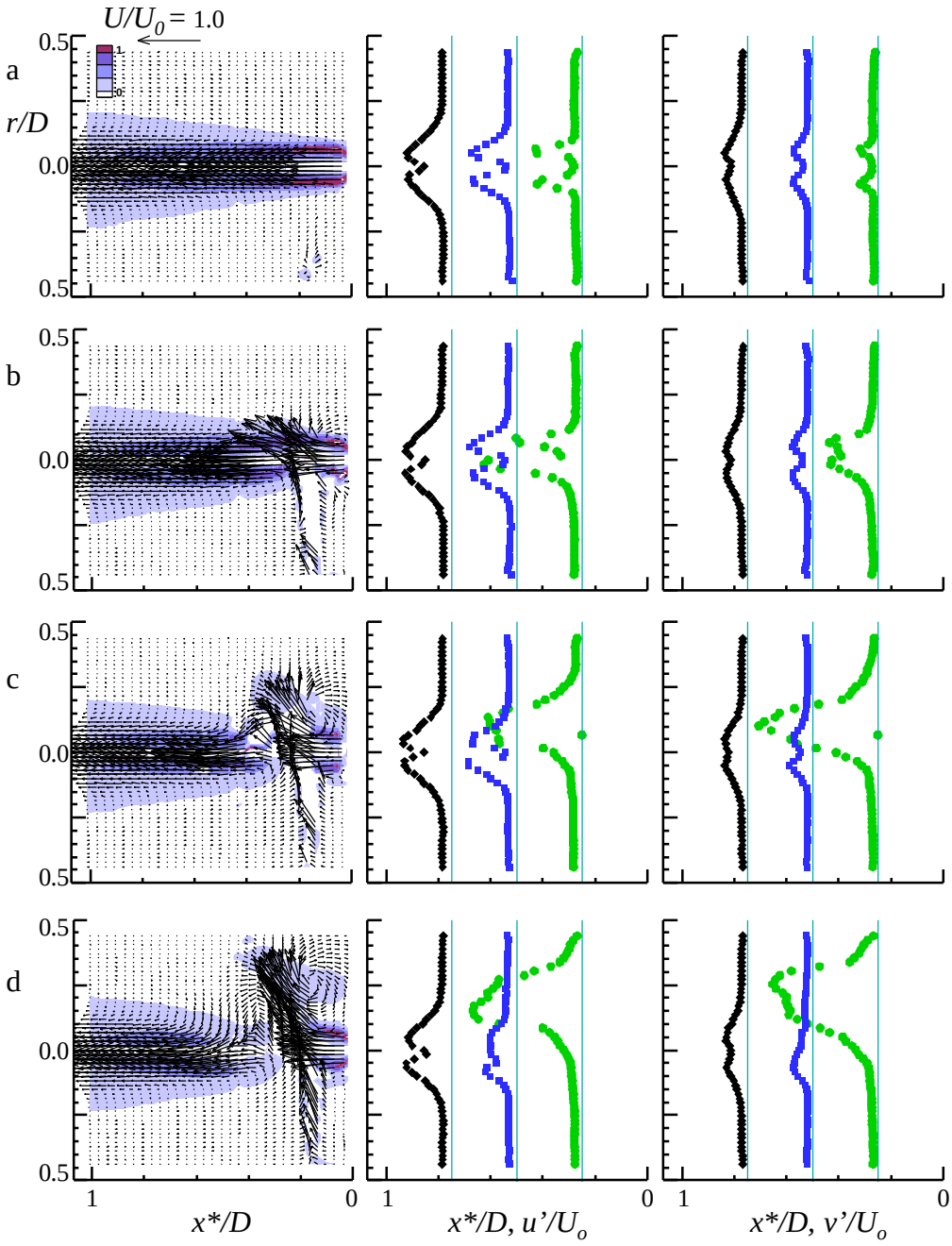

Figure 5.1 Maps of the phase-averaged normalized velocity, azimuthal-vorticity concentration, and cross-stream (radial) distributions of u'/U_o and v'/U_o in the domain $0.25 < x^*/D < 0.75$ at t = 0.27 (a), 0.77 (b), 1.02 (c), 1.27 (d), 1.77 (e), 2.27 (f), 2.77 (g), and 3.02 (h) ms after ignition, when the flow is forced with one actuator. Where U, u', and v' are scaled by U_o = 54.6 m/s, and the vorticity is scaled by W_o = 19100 sec^{-1}.

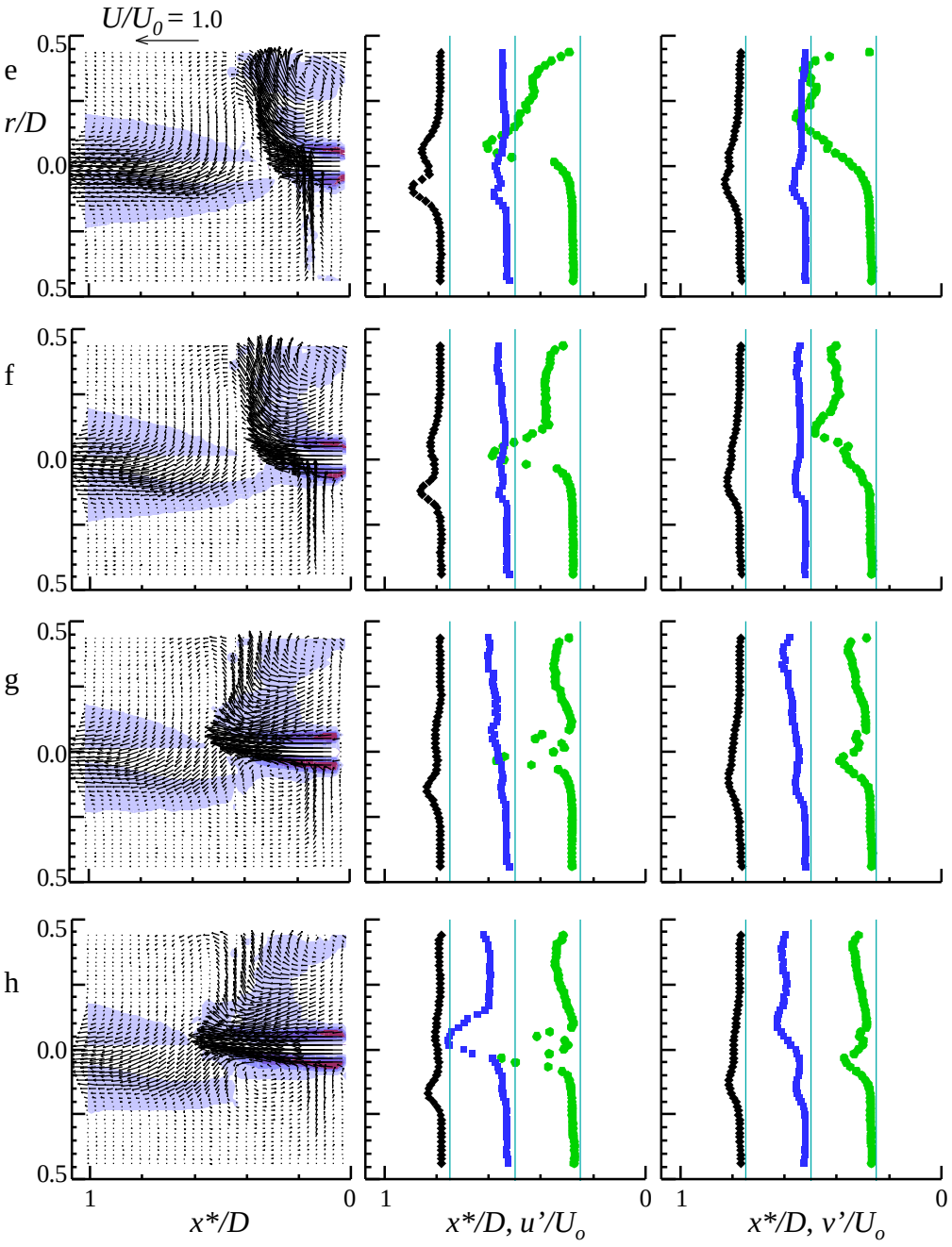

Figure 5.1 Continued

in the primary jet, ostensibly flows around the transient jet out of plane as is evident from the continued presence of the primary jet at $x^*/D > 0.2$. The flow structure comprised of the transient jet and the deflected portion of the primary jet (Figure 5.1d) drives a clockwise leading vortex, centered at $x^*/D = 0.15$ and $r/D = 0.25$, that appears to be part of a horseshoe vortex, which caries fluid from the annular flow towards the primary jet.

As the actuation jet weakens at $t \geq 1.77$ms (Figure 5.1e), the deflection of the primary jet begins to decrease, and for $t > 2.27$ms (Figure 5.1f-h), it begins to return to its original trajectory. Concurrently, the clockwise leading vortex becomes larger. Its center moves towards the annular tube, and it appears that ultimately it is advected with the return flow. The residual effects of the horseshoe vortex, which is now incoherent, are evident in the downward motion still present in the top half of Figures 5.1f and 5.1g for $x^*/D > 0.3$. As shown in Figure 5.1e, u' and v' at $x^*/D = 0.25$ for $0.0 < r/D < 0.15$ increase as the primary jet surges downward and forward. Meanwhile, u' and v' in the domain $0.0 < r/D < 0.15$ decrease at $x^*/D = 0.5$ and 0.75. It is noteworthy that as the primary jet returns to its original axial direction at $t > 2.77$ ms, a weak counter-clockwise vortex forms along its lower edge (Figures 5.1g and 5.1h). Concurrently, the cross-stream distributions of u' and v' begin to return to the original patterns.

The effects of actuation on the entire velocity field within the annular tube are illustrated in a sequence of vorticity concentration (W/W_o) maps (Figures 5.2a-e). These phase-averaged maps are acquired at a number of instances and only five are selected for Figure 5.2. At $t = 1.27$ ms after ignition (Figure 5.2a), the primary jet flow is disrupted

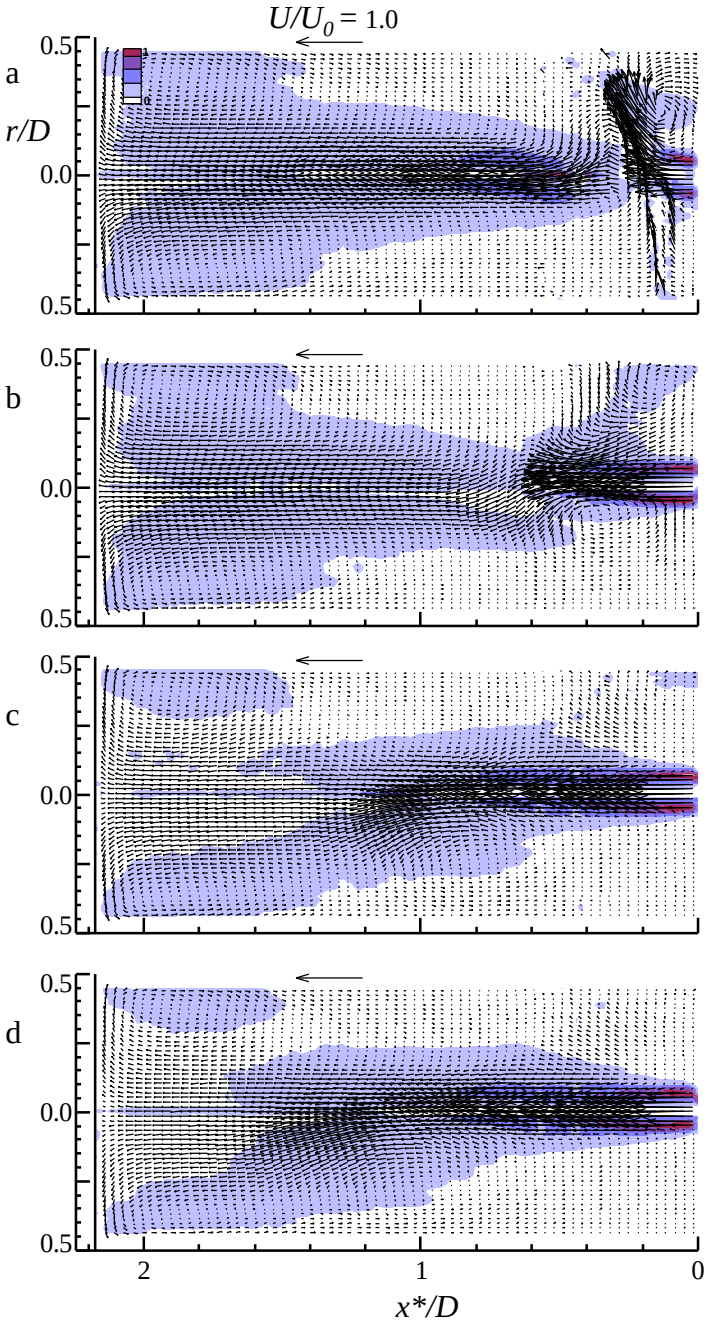

Figure 5.2 Maps of azimuthal-vorticity concentration in the domain $0.5 < x^*/D < 2.18$ at t = 1.27 (a), 3.27 (b), 6.27 (c), 8.27 (d), and 20.27 (e) ms after ignition. The vorticity is scaled by W_o = 19100 sec^{-1}.

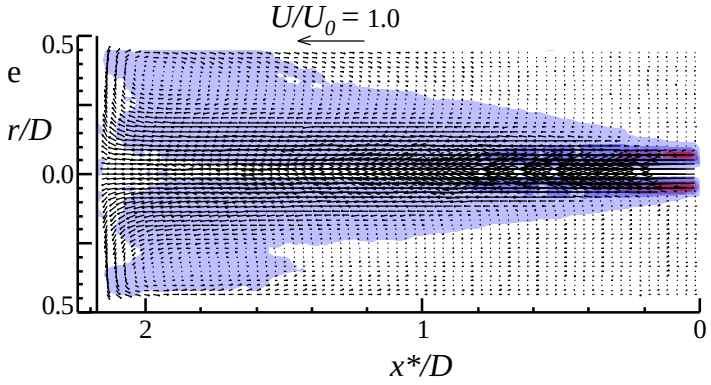

Figure 5.2 Continued

and becomes temporarily disconnected from the return flow. Downstream, the flow appears to be unaffected and continues its turn near the end-wall, driving a toroidal recirculation domain in the region $1.5 < x^*/D < 2.18$. Subsequently, at t = 3.27 ms after ignition (Figure 5.2b), the surge of the primary jet passes $x^*/D = 0.5$. The mean velocities downstream of the primary jet surge in the region $0.6 < x^*/D < 2.18$ are significantly reduced, due to the obstruction of the primary jet (Figure 5.2b). As shown in Figure 5.2b, the clockwise vortex, driven by the primary jet surge, becomes larger and occupies the region $0.2 < x^*/D < 0.5$ as it is advected by the return flow.

At t = 3.27 ms, the primary jet returns to its streamwise position and the flow within the tube is still reasonably axisymmetric (Figure 52.b). However, this symmetry is altered once the returning primary jet begins to overshoot (Figures 52.c and 52.d). Ultimately, the flow becomes distorted in the direction of motion of the primary jet (Figure 52.d) located in the region $0.6 < x^*/D < 1.2$ and $0.0 < r/D < 0.15$ as it passes $x^*/D = 1.0$ (Figure 5.5a). During the period between 8.27 ms (Figure 5.2d) and 20.27 ms

(Figure 5.2e), the primary jet returns to normal and the baseline flow is symmetric again in Figure 5.2e.

5.2 Forcing with Two Actuators Operating In-Phase

The response of the flow to diametrically-symmetric actuation is also investigated, using two opposing combustion actuators operating in phase at 10 Hz. Maps of the resulting phase-averaged velocity, azimuthal-vorticity concentration, and cross-stream distributions of u' and v' with the actuators operating in-phase are shown in Figures 5.3a-h. These phase-averaged data are obtained at equal time intervals between 0.27 and 3.27 ms after ignition.

Initially, the flow field still exhibits the characteristics of the baseline flow at t = 0.27ms (Figure 5.3a). Subsequently, at t = 0.77 ms (Figure 5.3b), the transient jets issuing from the actuators interact with the primary jet in the region $0.0 < x^*/D < 0.2$ and $0.0 < r/D < 0.15$ and form two coaxial, counter-flowing, jets (Figure 5.3b). The two transient jets act as a momentary obstruction, causing the primary jet to flow around them in a path out of the measurement plane. The blockage of the primary jet forms a wake (Figures 5.3b and 5.3c). At t = 0.77 ms (Figure 5.3b), the interaction with the transient opposing jets is characterized by a slight increase of u' in the domain $0.05 < r/D < 0.15$ and substantial increase of v' in the domain $0.0 < r/D < 0.1$ at (x^*/D = 0.25). Figure 5.3c shows make up fluid flowing radially into the wake domain downstream of the actuator

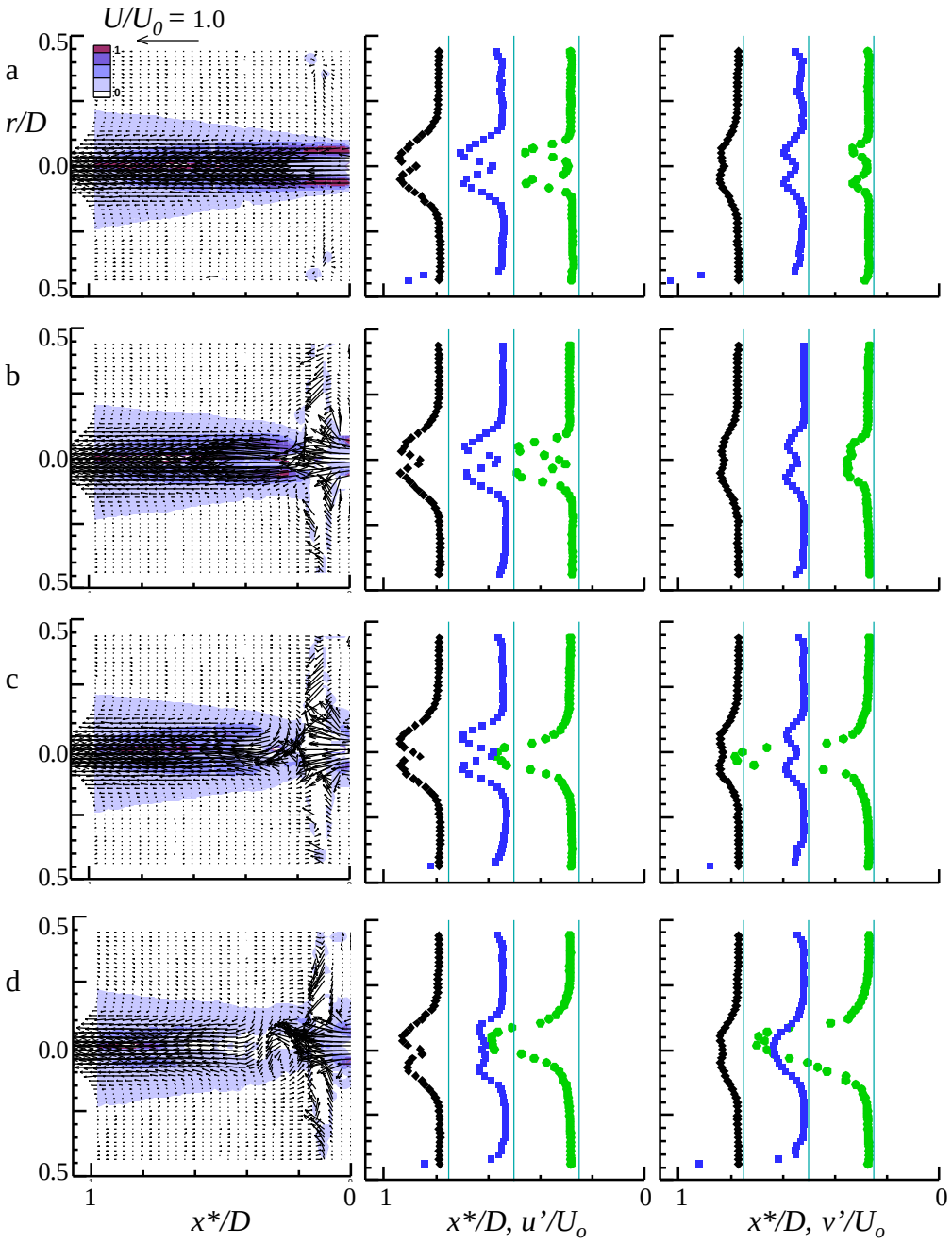

Figure 5.3 Maps of the phase-averaged normalized velocity, azimuthal-vorticity concentration, and cross-stream (radial) distributions of u'/U_o and v'/U_o in the domain $0.25 < x^*/D < 0.75$ at t = 0.27 (a), 0.77 (b), 1.02 (c), 1.27 (d), 1.77 (e), 2.27 (f), 2.77 (g), and 3.27 (h) ms after ignition when the flow is forced with two actuators operating in phase. Where U, u', and v' are scaled by U_o = 54.6 m/s, and the vorticity is scaled by W_o = 19100 sec^{-1}.

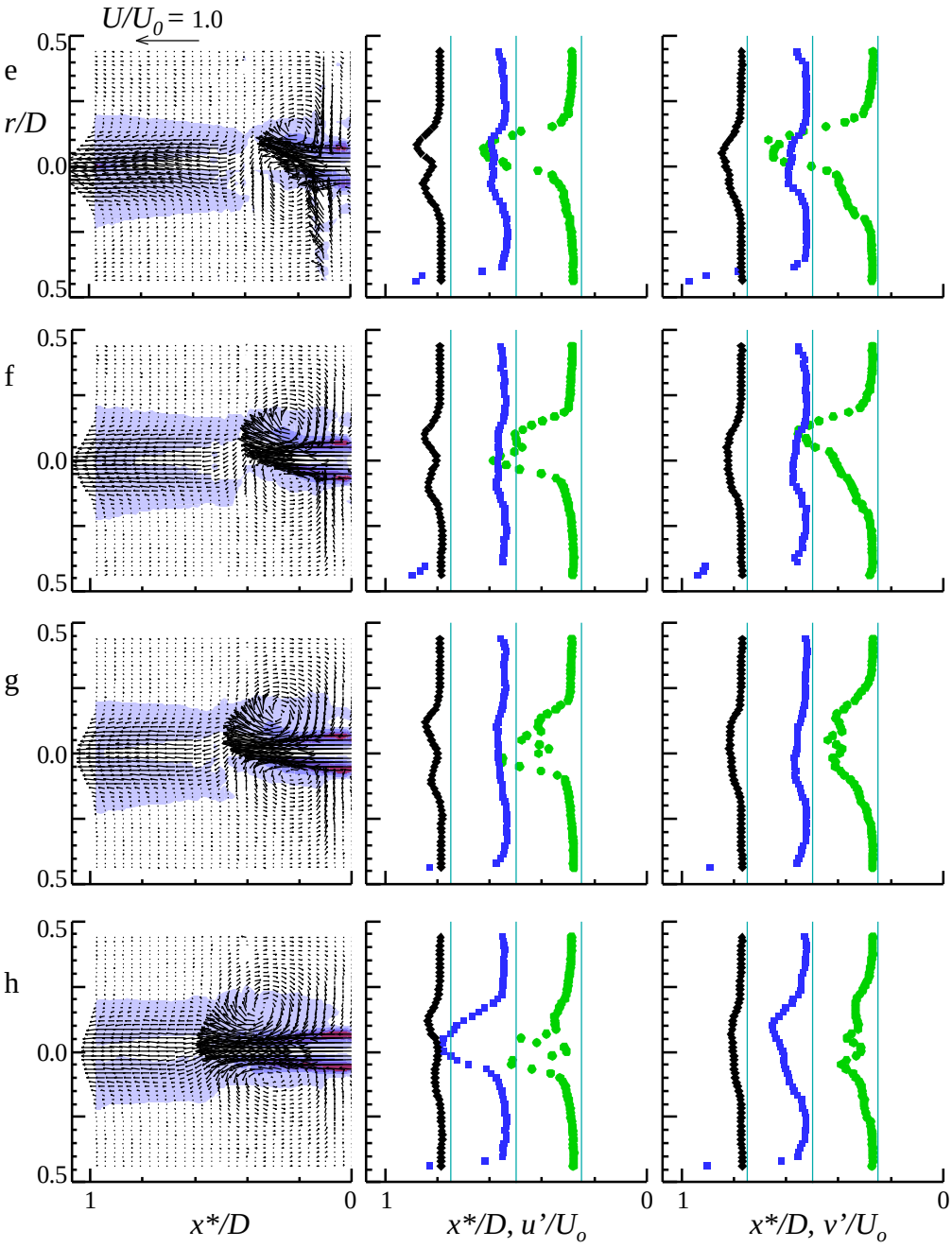

Figure 5.3 Continued.

jets. At this time, u' and v' attain high values [$u' \sim O(0.3U_o)$ & $v' \sim O(0.55U_o)$] at $x^*/D = 0.25$.

For $t = 1.27$ ms (Figure 5.3d), the primary jet begins to break through the transient jets forming a counter-clockwise circulation domain, which suggests that the strengths of the actuation jets are not matched exactly. This counter-clockwise circulation domain generates additional turbulence and draws additional fluid from the return flow into the primary jet. When the actuator jets vanish ($t > 2.27$ ms), the primary jet begins to flow and forms two counter-rotating vortices (Figure 5.3e). The counter-clockwise vortex is weaker than the clockwise vortex, owing to the slight asymmetry of the actuation. These vortices recirculate fluid between the return flow and the primary jet. The flow associated with the restarting primary jet becomes more symmetric at $t > 2.77$ ms (Figure 5.3h). The streamwise motion of these vortices is associated with a substantial peak in u' and a somewhat lower peak in v'. The circulation domains, generated by the interaction of the primary jet with the two opposing actuator jets at $0.2 < x^*/D < 0.4$ (Figure 5.3c), circulate fluid from the return flow into the primary jet. The fluid drawn from the return flow mixes with the primary jet. Furthermore, additional azimuthal flapping in the primary jet causes additional mixing between the primary jet and the return flow.

The surge, induced by the actuation, is observed in more detail further downstream in the domain $0.9 < x^*/D < 1.28$ (Figure 5.4). These measurements are taken in three overlapping (top, center and bottom) 28 mm x 28 mm windows, located 76 mm downstream (in the positive x^* direction) of the jet tube. The resolution for these data sets is 28 μm/pixel, and the frame-pair time delays are 15 μs at the center and 4 μs at the top/bottom windows.

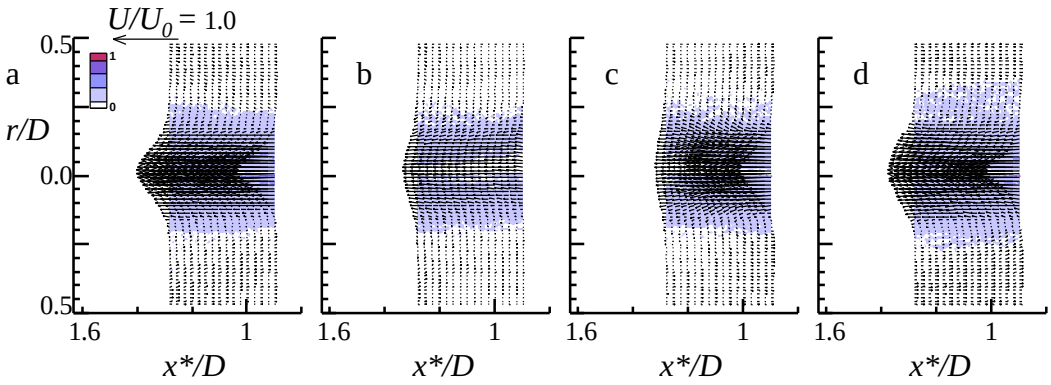

Figure 5.4 Maps of the phase-average normalized velocity and azimuthal-vorticity concentration in the domain $0.9 < x^*/D < 1.28$ for two actuators operating in phase at t = 1.27 (a), 4.27 (b), 6.27 (c), and 8.27 (d) ms after ignition. Where U is scaled by U_o = 54.6 m/s, and vorticity is scaled by W_o = 19100 sec^{-1}.

Figure 5.4a shows the velocity distribution before the onset of the transitory flow. This flow slows considerably in Figure 5.4b, and the vorticity concentrations appear to be advected radially away from the centerline. When the jet flow returns (Figure 5.4c), an increased mass flux is observed on the right, which indicates that there is also an increase in the flux of the return flow. This increase propagates to the left (Figure 5.4d), indicating that the transients affect both the forward and return flows, and therefore, the mixing between them.

5.3 Consecutive, Pulsed Actuation

The present experiments also considered the effect of a controlled delay between the two actuators. Specifically, the actuators are set to operate with a time delay of 1.5 ms. The data in Figures 5.5a-h show the interaction between the actuation jets and the

primary jet for $0.27 < t < 5.27$ ms following the ignition of the first (bottom) actuator. The bottom actuator in Figure 5.5 is fired first, and its effect on the flow within the first 1.5 ms is the same as in Figure 5.1 (single actuator). The blank region at $0.55 < x^*/D < 0.7$ indicates a region in which no data could be acquired due to glare and reflections.

At $t = 1.77$ ms (Figure 5.5b), the effect of the blockage of the primary jet and the penetration of the bottom jet are quite apparent. As noted above, the top jet is actuated at $t = 1.5$ ms and its operation is effectively over by $t = 4.27$ ms in Figure 5.5f. The top jet interacts with the protrusion, produced by the bottom jet, and apparently pushes this flow downward (i.e. below the tube centerline), as is also evident by the rms fluctuations u' and v' in Figures 5.5c and 5.5d. As is evident in Figure 5.5d, the second actuator jet also displaces some of the primary jet fluid downward. The interaction with the second actuator jet and the recovery of the primary jet form a counter-clockwise vortex in the lower half of the annular tube, which is part of a horseshoe vortex that draws fluid upward into the primary jet, shown in Figures 5.5e-h. This (horseshoe) vortex is apparently sheared by the motions of the primary jet and the return flow, and its cross-section becomes elongated in the flow direction. The presence of this vortex is also evident in the cross-stream distributions of the rms velocity fluctuations (eg. Figure 5.5f – 5.5h).

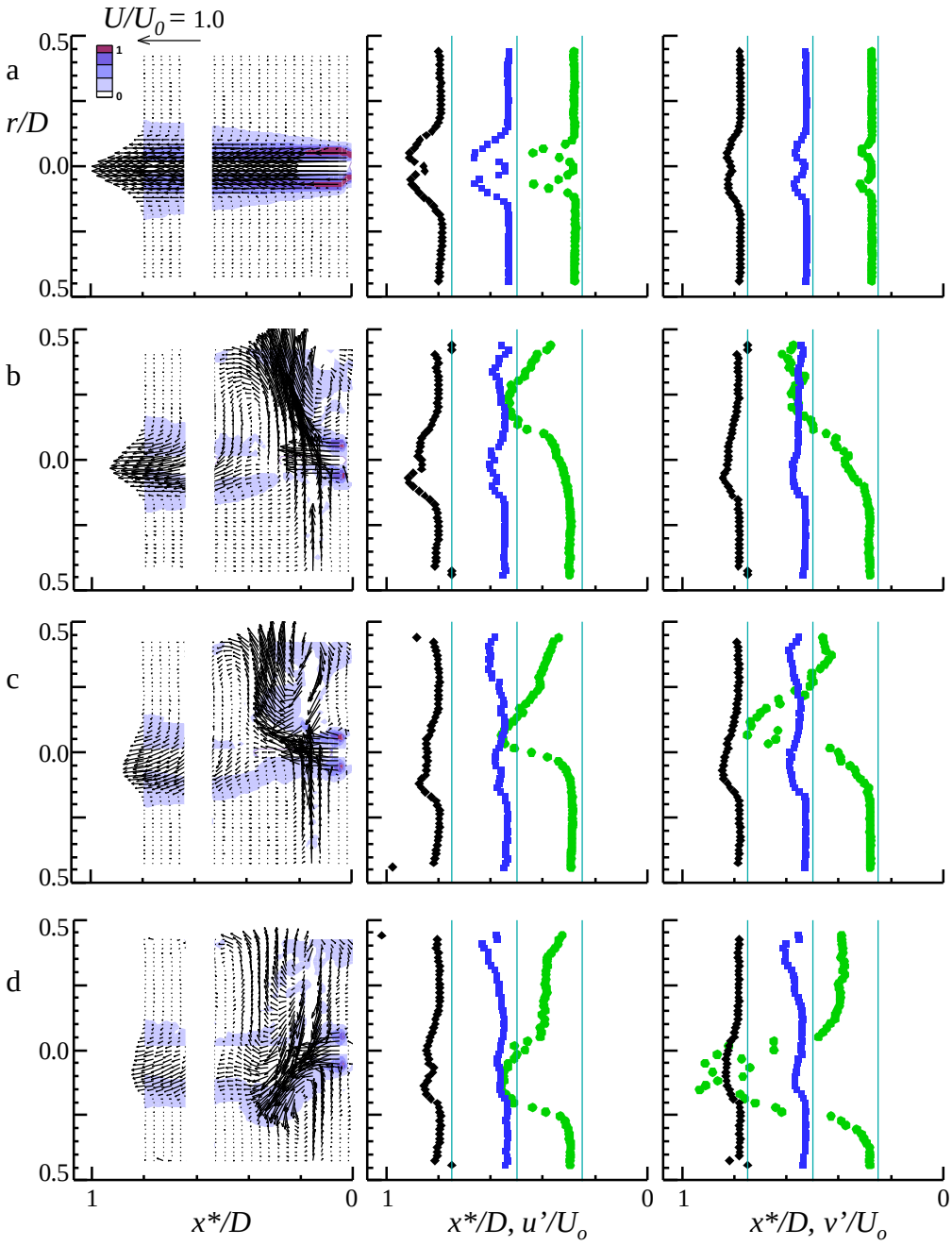

Figure 5.5 Maps of the phase-averaged normalized velocity, azimuthal-vorticity concentration, and cross-stream (radial) distributions of u'/U_o and v'/U_o in the domain $0.25 < x^*/D < 0.75$ at t = 0.27 (a), 1.77 (b), 2.27 (c), 2.77 (d), 3.77 (e), 4.27 (f), 4.77 (g), and 5.27 (h) ms after the ignition of the bottom actuator when the flow is forced with two actuators operating 1.5 ms out of phase. Where U, u', and v' are scaled by U_o = 54.6 m/s, and the vorticity is scaled by W_o = 19100 sec^{-1}.

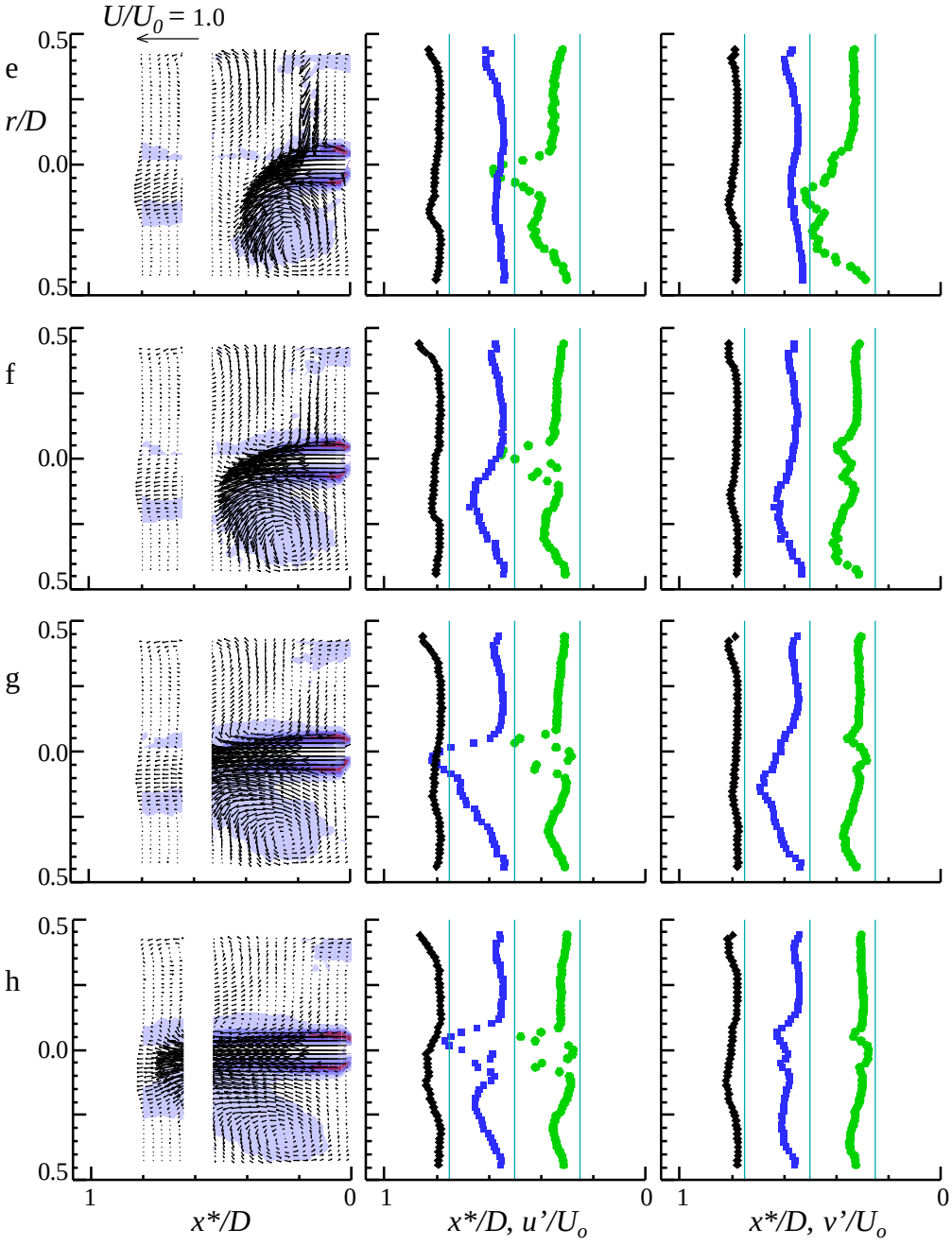

Figure 5.5 Continued

The response of the flow field in the domain $0.9 < x^*/D < 1.28$ to the time delayed actuation is shown in Figures 5.6a-d for t = 1.27, 5.27, 7.27, and 9.27 ms, respectively. The measurements are similar to the ones shown in Figure 5.4. These data show how the flow of the primary jet (Figure 5.6a) is interrupted (Figure 5.6b, t = 5.27 ms), resumes at t = 7.27 ms (Figure 5.6c), and becomes fully established by t = 9.27 ms (Figure 5.6d). Furthermore, while the actuator jet is active, the primary jet flows around the actuator jet (i. e. out of the measurement plane) and the return flow is sheared somewhat. It is also noteworthy that these data show very little radial motion of the primary jet flow within this domain, even though, the actuation leads to strong radial motion near the jet origin.

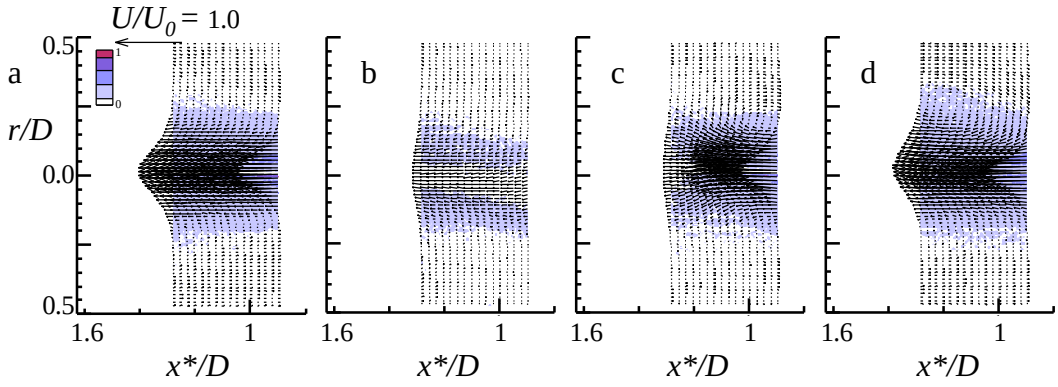

Figure 5.6 Maps of the phase-average normalized velocity, and azimuthal-vorticity concentration in the domain $0.9 < x^*/D < 1.28$ for two actuators operating 1.5 ms out of phase at t = 1.27 (a), 5.27 (b), 7.27 (c), and 9.27 (d) ms after ignition of the bottom actuator. Where U is scaled by U_o = 54.6 m/s, and vorticity is scaled by W_o = 19100 sec^{-1}.

The present data shows that when the flow is forced by two actuators operated in-phase the most significant increase in rms velocity fluctuations occurs near the center line $r/D < 0.15$. When a single actuator or two delayed actuators are used, the most significant increase in rms velocity fluctuations occurs off the centerline in the domain $0.15 < r/D < 0.35$.

5.4 Time Traces of the Pressure

Time traces of the static pressure p are measured on the end-wall of the outer tube. The pressure ports are located on the centerline and on four equally spaced arcs along the periphery of the circle $r = 0.25D$ (Figure 3.8b). These data are normalized by the stagnation pressure of the primary jet (P_s~1.7 kPa). The spark that ignites the actuators generates a brief noise spike in the time series of the pressure measurements. This spike appears about 10 ms following the data trigger and is evident in the pressure time traces prior to the arrival of the flow transient that is associated with actuation.

The time traces of the pressure measured at the center port of the end-wall show the transient response when a single actuator is operated at 10 Hz for L = 102, 152, and 255 mm (Figures 5.7a, 5.8a, and 5.9a). As shown in Figure 5.7a, for L = 102 mm, p increases to $0.46P_s$ ($0.14P_s$ above the baseline pressure) at r/D = 0 at 1.5 ms after the ignition (at 10ms). For L = 102 mm, a pressure pulse would take 0.3 ms to travel from the axial position of the actuator orifices to the end-wall. The plume of the actuator jet reaches its maximum size 1.27 ms after ignition (Figure 5.1d). Hence, the pressure rise apparently corresponds to the displacement of the fluid within the annular tube due to the evolution of the actuator jet. However, the subsequent reduction in jet speed, due to the blockage by the actuator jet, is accompanied by a momentary reduction in pressure before the pressure recovers to its (steady-state) amplitude. The increase in p is accompanied by an oscillation at a nominal frequency of 400 Hz, which appears to be associated with a resonance of the tube system.

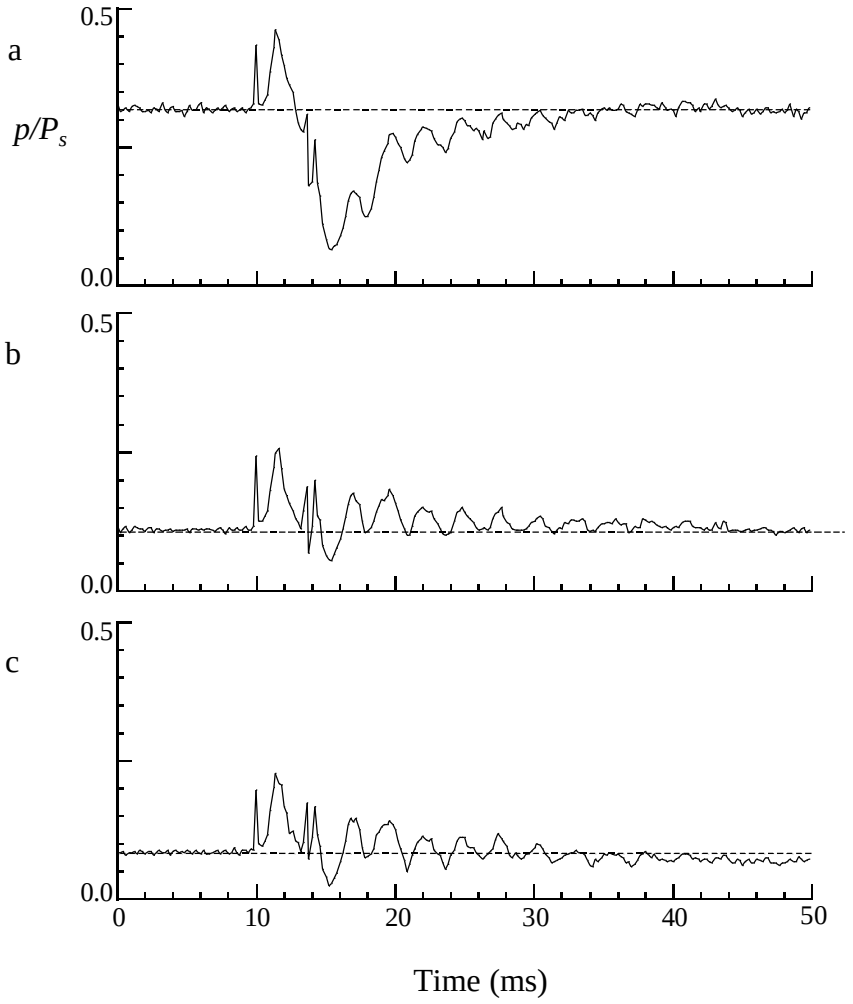

Figure 5.7 Time traces of the pressure at the end-wall when the actuator is operated at 10 Hz at r/D = 0 (a) and r/D = 0.25 at ports #1 (b) and #2 (c) for L = 102 mm (U_o = 53.5 m/s).

The corresponding pressure traces at r/D = 0.25 at ports #1 and #2 are shown in Figures 5.7b and 5.7c. These traces are very similar and indicate that the actuated flow is axisymmetric downstream of the actuator jets. These traces show the onset of the transient and indicate a high frequency oscillation (about 2 kHz) before the global tube oscillation (400 Hz) commences. It is noteworthy that the global oscillation decays within about 30 ms.

When L = 152 mm (Figure 5.8a), the transient increase in pressure, associated with the initial perturbation, is very similar to that shown in Figure 5.7a. The reduction in pressure, due to the slow down in the primary jet speed, is smaller than for L = 102 mm, presumably due to added compressibility within the return tube. The oscillation frequency during pressure recovery, which is somewhat lower, is 330 Hz (presumably due to the increase in tube length). The time traces measured at ports #1 and #2 (Figure 5.8b and 5.8c) are very similar to those for the corresponding ports in Figure 5.7.

Finally, when L = 255mm (Figure 5.9), the transient associated with the actuation is evident only by the presence of the perturbation, and the magnitude is smaller than for the shorter tube lengths. In addition, the decrease in pressure (of Figure 5.7) is absent, and the magnitude of the oscillation that follows the transient is minimal. It appears that the reduced pressure transients are associated with increased system damping and the fact that most of the flow turns back before reaching the end-wall when $L/D \geq 2.9$.

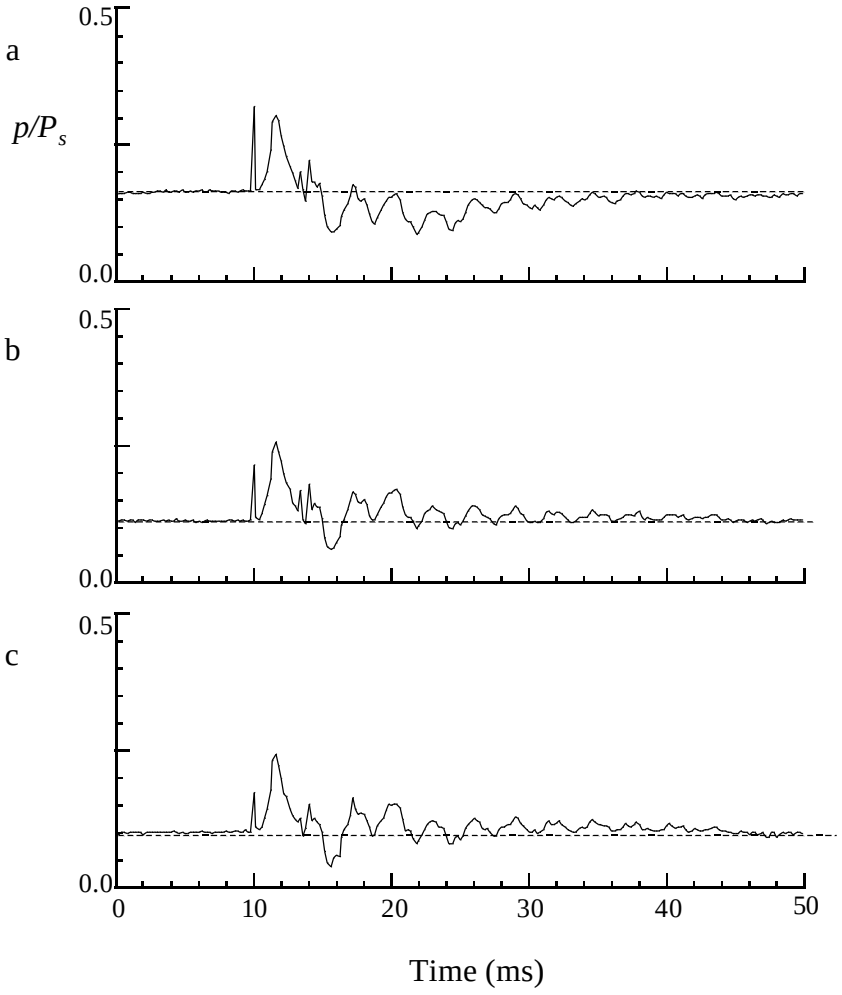

Figure 5.8 Time traces of the pressure at the end-wall when the actuator is operated at 10 Hz at r/D = 0 (a) and r/D = 0.25 at ports #1 (b) and #2 (c) for L = 152 mm (U_o = 53.5 m/s).

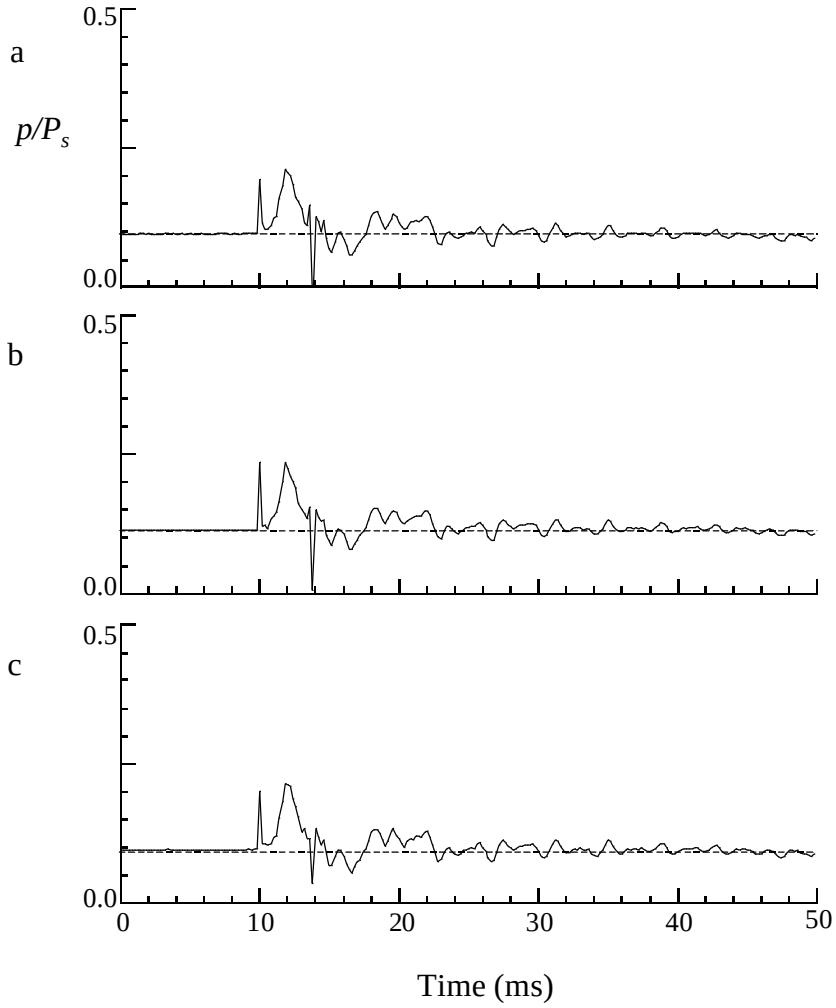

Figure 5.9 Time traces of the pressure at the end-wall when the actuator is operated at 10 Hz at r/D = 0 (a) and r/D = 0.25 at ports #1 (b) and #2 (c) for L = 255 mm (U_o = 53.5 m/s).

The initial increase in p at all locations along the end-wall is generated by the evolution of the transient jet issuing from the combustion driven actuator. The subsequent fluctuations of p are ostensibly due to a resonance of the air column within the annular tube. This global oscillation persists for 30 ms, indicating that operation of the actuators at a frequency above 34 Hz would drive a continuous 400 Hz oscillation within this system.

CHAPTER 6

CONCLUSIONS

The present work reports on a countercurrent flow in a dead-end tube with and without momentary pulsed cross-stream jets for flow control. These jets are produced by combustion driven actuators. The flow within the dead-end tube is driven by an axisymmetric jet that is aligned with the tube's centerline. The baseline flow, in the absence of actuation, is studied using particle image velocimetry for configurations in which d/D = 0.127 and L/D = 0.726, 1.45, 2.18, and 3.64 for both Re_d = 3.12 x10^4 and 1.50 x10^4. Actuation is applied for L/D = 2.18 and Re_d = 3.12 x10^4. The actuators are operated at 10 Hz with a stoichiometric mixture, yielding C_{mav} = 1.4 x10^{-2}. The primary flow is forced by one or two radially mounted actuators; when two actuators are used, they are operated either simultaneously or at 1.5 ms delay.

The analytical solution describing the mean velocity field of the unforced flow given by Abramovich (1963) indicates that the shape of the velocity contour U = 0 generally varies with d/D, but that in the domain $x^*/R > 2.8$ ($x^*/D > 1.4$) the contour U = 0 is identical for all d/D, and independent of the Reynolds number. However, Abramovich's model is derived for a generic long, axisymmetric dead-end tube, hence his model does not address the variation with L/D. The present data indicate that this contour is at most a weak function of the Reynolds number, but it varies with L/D. In particular, the streamwise rate at which the contour U = 0 widens in the near-field increases as L/D decreases. However, as L/D decreases, the return flow counterbalances the natural spreading of the primary jet, resulting in a reduction of the streamwise half-

spreading angle. These observations indicate that the region associated with low velocity expands as L/D decreases, suggesting increased momentum exchange and mixing between the jet flow and the return flow. As a result of impingement, a toroidal recirculation domain is formed, as reported by White et al. (1975). Calculations of the mass flux through the axial cross-sections of the return tube suggest that the recirculation rate for a long dead-ended tube is below that which is expected based on the analytical solution and increases with decreasing L/D.

A potential core (similar to that observed for conventional round jets) is evident in the domain $0.0 < x^*/D < 0.5$ ($0.0 < x^*/d < 3.9$) for all values of L. The jet core in an annular-return configuration is somewhat smaller than the jet core for a free, turbulent jet impinging on a flat plate for $Re_d > 4000$. For both jet speeds tested here, the (normalized) centerline velocity downstream of the potential core decreases as $x^{*\,-1.2}$, which is higher than the rate for a free turbulent jet ($x^{*\,-1}$). The values of the centerline velocity, calculated by using the analytical solution (Abramovich, 1963), exceed the experimental values by as much as 20 – 50% in the domain $x^*/D > 1$, due to the absence of viscous effects in the model.

Measurements near the end-wall show that the instantaneous flow field is highly unstable and " flaps" within the tube so that the primary stagnation point on the end-wall meanders about the geometric centerline. The radial flapping of the primary jet drives a time-dependant redistribution of the flow in the annular domain that must be balanced. This is also evident by the streamwise (x^*) increase in turbulence intensity within the annular region. In fact, the velocity fluctuations in the return flow are on the order of the mean velocity.

The characteristics of the vorticity field and the pressure distribution along the end-wall imply that, when $L/D \leq 2.18$, the primary jet impinges on the end-wall and turns to form the return (exhaust) flow. The annular-return flow and the primary jet form the toroidal recirculation domain. When $L/D \geq 2.9$, the primary jet barely reaches the end-wall and turns very slowly, as more and more of the fluid turns before reaching the end-wall. Pressure distributions for $L \geq 2.9$ are basically uniform and the terminal stagnation pressure is $O[0.1P_s]$ (higher than the prediction by the numerical simulations of Amano (1986)).

When a single actuator is used to force the flow; the transient actuator jet acts as a momentary obstruction for the primary jet and forces the primary jet to flow around it. As the transient jet reaches its maximum strength, the primary jet fluid is deflected toward the annular surface and some of it apparently flows around the transient jet (out of plane). Interaction with the primary jet results in a substantial increase of the velocity fluctuations and leads to the formation of a horseshoe vortex in the annular region. The (horseshoe) vortex draws fluid (a mixture of exhaust and primary jet fluid) from the annular region into the primary jet. Similarly, it is anticipated, that the primary jet fluid out-of-plane also interacts with and entrains exhaust fluid into the primary jet. As the transient jet weakens, the primary jet surges forward and the baseline flow is reestablished. This jet surge is characterized by a high-velocity front, having high-amplitude velocity fluctuations, and is preceded by a low-velocity front.

When two opposite actuators are operating in-phase, the transient jets act as a symmetric obstruction, and more of the primary jet flow is deflected out of plane. The interaction between the three jets generates a circulation domain that draws additional

fluid from the annular region into the primary jet. When the flow is forced (triggering the actuators at a 1.5 ms delay), the primary jet is deflected twice before it can return to its original flow direction.

When the flow is forced by two actuators operated in-phase, the greatest increase in the velocity fluctuations (and hence the rate of mixing) occurs within the primary jet. On the other hand, when a single actuator or two actuators operating out-of-phase are used to force the flow, the greatest increase in the velocity fluctuations (and hence the rate of mixing) occurs in the annular region. Furthermore, when a single actuator or two out-of-phase actuators are used, the vortices draw fluid (which is already a mixture of the newly injected and exhaust fluid) into the primary jet, where it mixes with the remnant of the primary-jet fluid that was not deflected.

Since the mixture ratios of recirculated fluid to newly injected fluid cannot be determined from the present data, it is impossible to determine which configuration is the best for improving recirculation. It appears that the high-velocity and low-velocity fronts generate an effect similar to the propagation of a pulse or shock. For a given primary-jet speed, an important parameter of the actuation period is the distance between the end-wall and the exit plane of the primary jet. Proper selection of the actuation repetition rate can lead to flow oscillations owing to feedback, which can be adjusted by the distance between the injection plane and the end-wall.

In conclusion, combustion-driven actuators exhibit substantial control authority in the vectoring of relatively large-diameter, medium-velocity jets and generate large-scale flow instabilities. However, the exhaust gas recirculation that is generated by the baseline

flow within the dead-end tube is very large when $d/D \leq 0.127$ and therefore, the response to forcing by the actuators may not improve the performance in this configuration.

REFERENCES

Abramovich, G.N. (1963). *The Theory of Turbulent Jets.* Cambridge: The MIT Press. pp. 444-474

Amano, R.S. (1986). "A Numerical Study of Turbulent Axisymmetric Jets Flowing Into Closed Tubes." ASME Journal of Energy Technology, Vol.. 108, pp. 286-290.

Bruno, C. and Vallini, L. (1999). "Flameless Combustion And Its Application To Aeroengines." International Society for Air Breathing Engines & AIAA Paper No. ISABE 99-7099 / A99-34100.

Batchelor, G. K., (1956). " On Steady Laminar Flow With Closed Streamlines at Large Reynolds Numbers." Journal of Fluid Mechanics. Vol. 1 pp. 177-190

Batchelor, G. K., (1956). "A Proposal Concerning Laminar Wakes Behind Bluff Bodies at Large Reynolds Number." Journal of Fluid Mechanics. Vol. 1 pp. 388-398

Crittenden, T., Glezer, A., Funk, R., and Parekh, D.(2001). "Combustion-Driven Jet Actuators for Flow Control." AIAA Paper No.2001-2768.

Crittenden, T.(2003). "Fluidic Actuators for High Speed Flow Control." PhD Thesis, Georgia Institute of Technology. Atlanta, Ga

Funk, R., Parekh, D., Crittenden, T., and Glezer, A. (2002). "Transient Separation Control Using Pulsed Combustion Actuation." AIAA Paper No.2002-3166.

Eckmann, D.M., Fogg, N.R., Frerichs, T.A., and Lueptow, R.M. (1996). "Laminar Jet Flow Into A Dead-end Tube." ASME Fluids Engineering Division, Vol.. 237, pp. 667-672.

Hrycak, P., Lee, D.T., Gauntner, J.W., and Livingood, J.N.B. (1970). "Experimental Flow Characteristics of a Single Turbulent Jet Impinging on a Flat Plate." NASA TN D-5690

Landreth, C.C., and Adrian, RJ (1990). "Impingement of a low Reynolds number circular jet onto a flat plate at normal incidence." Experiments in Fluids, Vol. 9, pp.74-84

Raffel, M., Willert, C. and Kompenhans, J. (1998). *Particle Image Velocimetry*. Berlin, Germany: Springer.

Rajaratnam, N. (1976). *Turbulent Jets*. San Diego: Elsevier Press.

White, W.N., Darooka, D.K., and Sogin, H.H. (March 1975). “On Recirculating Flow in a Dead-End Vessel.” ASME Fluids Engineering Division, pp. 119-120.

Ueda, T., Imaizumi, H., Mizomoto, M., and Shepherd, I.G. (1996). “Velocity statistics along the stagnation line of an axisymmetric stagnating turbulent flow.” Experiments in Fluids, Vol. 22, pp. 473-481